ALLSENSORS 2022

The Seventh International Conference on Advances in Sensors, Actuators, Metering and Sensing

ISBN: 978-1-61208-987-4

June 26th – 30th, 2022

Porto, Portugal

ALLSENSORS 2022 Editors

Matteo Tonezzer, CNR-IMEM, Trento, Italy

Almudena Rivadeneyra, Universidad de Granada, Spain

ALLSENSORS 2022

Forward

The Seventh International Conference on Advances in Sensors, Actuators, Metering and Sensing (ALLSENSORS 2022), held in Porto, Portugal, June 26 - 30, 2022., covered related topics on theory practice and applications of sensor devices, techniques, data acquisition and processing, and on wired and wireless sensors and sensor networks.

Sensor networks and sensor-based systems support many applications today above ground. Underwater operations and applications are quite limited by comparison. Most applications refer to remotely controlled submersibles and wide-area data collection systems at a coarse granularity. Other remote sensing domains and applications are using special sensing devices and services. Transducers and actuators complement the monitoring and control and constitute an area of interest related to sensors. They make use of specific sensor-based measurements and convey appropriate control actions.

ALLSENSORS 2022 was intended to serve as a forum for researchers from the academia and the industry, professionals, standard developers, policy makers, investors and practitioners to present their recent results, to exchange ideas, and to establish new partnerships and collaborations. The accepted papers covered a large spectrum of topics on techniques and applications, best practices, awareness and experiences as well as future trends and needs (both in research and practice) related to all aspects of sensor-based applications and services.

We take here the opportunity to warmly thank all the members of the ALLSENSORS 2022 technical program committee as well as the numerous reviewers. The creation of such a broad and high quality conference program would not have been possible without their involvement. We also kindly thank all the authors that dedicated much of their time and efforts to contribute to the ALLSENSORS 2022. We truly believe that thanks to all these efforts, the final conference program consists of top quality contributions.

This event could also not have been a reality without the support of many individuals, organizations and sponsors. In addition, we also gratefully thank the members of the ALLSENSORS 2022 organizing committee for their help in handling the logistics and for their work that is making this professional meeting a success.

We hope the ALLSENSORS 2022 was a successful international forum for the exchange of ideas and results between academia and industry and to promote further progress on the topics of sensors. We also hope that Porto provided a pleasant environment during the conference and everyone saved some time for exploring this beautiful city

ALLSENSORS 2022 Chairs

ALLSENSORS Steering Committee
Michael Niedermayer, Berliner Hochschule für Technik (BHT), Germany
Paulo E. Cruvinel, Embrapa Instrumentation, Brazil
Matteo Tonezzer, CNR-IMEM, Trento, Italy
Almudena Rivadeneyra, Universidad de Granada, Spain
Sandrine Bernardini, Aix Marseille University, France

ALLSENSORS 2022 Publicity Chair
Laura Garcia, Universitat Politècnica de València (UPV), Spain
José Miguel Jiménez, Universitat Politecnica de Valencia, Spain

ALLSENSORS 2022

COMMITTEE

ALLSENSORS Steering Committee

Michael Niedermayer, Berliner Hochschule für Technik (BHT), Germany
Paulo E. Cruvinel, Embrapa Instrumentation, Brazil
Matteo Tonezzer, CNR-IMEM, Trento, Italy
Almudena Rivadeneyra, Universidad de Granada, Spain
Sandrine Bernardini, Aix Marseille University, France

ALLSENSORS 2022 Publicity Chair

Laura Garcia, Universitat Politècnica de València (UPV), Spain
José Miguel Jiménez, Universitat Politecnica de Valencia, Spain

ALLSENSORS 2022 Technical Program Committee

Francesco Aggogeri, University of Brescia, Italy
Otman Aghzout, National School of Applied Sciences of Tetouan, Morocco
Amin Al-Habaibeh, Nottingham Trent University, UK
Ammar Al-Jodah, Monash University, Australia
Youssef N. Altherwy, Imperial College London, UK
Kawiwat Amnatchotiphan, Rangsit University, Thailand
Darius Andriukaitis, Kaunas University of Technology, Lithuania
Piotr Artiemjew, University of Warmia and Mazury, Poland
Farzad Asgarian, University of Michigan, Ann Arbor, USA
Herve Aubert, Laboratory for Analysis and Architecture of Systems (LAAS-CNRS), France
Roberto Beghi, Università degli Studi di Milano, Italy
Artur Bejger, Maritime University of Szczecin, Poland
Fateh Benmahmoud, Grenoble-INP. - Université Grenoble-Alpes, France
Roc Berenguer Pérez, TECNUN - Technological Campus of the University of Navarra, Spain
Sandrine Bernardini, Aix Marseille University, France
Mourad Bezzeghoud, University of Évora, Portugal
Xavier Boddaert, Mines Saint Etienne | Centre Microélectronique de Provence (CMP), France
Muhammad Ali Butt, Warsaw University of Technology, Poland
Ismail Butun, Chalmers University of Technology, Sweden
Maria Candelaria Hernandez Goya, Universidad de La Laguna, Spain
Juan Vicente Capella Hernández, Universitat Politècnica de València, Spain
Vítor Carvalho, 2AI-EST-IPCA / Algoritmi Research Centre - UM, Portugal
Paula María Castro Castro, Universidade da Coruña, Spain
Rosario Catelli, Institute for High Performance Computing and Networking (ICAR) - National Research Council (CNR), Italy
Debashish Chakravarty, IIT Khaargpur, India
Nan-Fu Chiu, National Taiwan Normal University,Taiwan
Susana Costa, University of Minho, Portugal
Paulo E. Cruvinel, Embrapa Instrumentation, Brazil

Francesco G. Della Corte, University of Napoli Federico II, Italy
Emiliano Descrovi, Polytechnic University of Turin, Italy
Chérif Diallo, Université Gaston Berger (UGB), Senegal
Yvan Duroc, University Claude Bernard Lyon 1, France
Attilio Frangi, Politecnico di Milano, Italy
Orlando Frazão, INESC TEC, Porto, Portugal
Kelum Gamage, University of Glasgow, UK
Jiechao Gao, University of Virginia, USA
Félix J. García Clemente, University of Murcia, Spain
Pietro Garofalo, Turingsense EU LAB s.r.l., Italy
Mojtaba Ghodsi, University of Portsmouth, UK
Patrick Goh, Universiti Sains Malaysia, Malaysia
Sanaz Haddadian, Heinz Nixdorf Institute | University of Paderborn, Germany
Kuan He, Apple Inc., USA
Daniel Hill, Aston University, UK
Carmen Horrillo-Güemes, Grupo de Tecnología de Sensores Avanzados (SENSAVAN) | ITEFI-CSIC, Madrid, Spain
Rui Igreja, Universidade NOVA de Lisboa, Portugal
Dimosthenis Ioannidis, CERTH/ITI, Thessaloniki, Greece
Ahmed Abu Ismaiel, Municipality of Abasan Al-Kabira, Gaza, Palestine
Nikos Kalatzis, Neuropublic S.A. / National Technical University of Athens, Greece
Grigoris Kaltsas, University of West Attica, Greece
Liuwang Kang, University of Virginia, USA
M-Tahar Kechadi, University College Dublin (UCD), Ireland
Anwesha Khasnobish, TCS Research, Kolkata, India
Jan Kubicek, VSB - Technical University of Ostrava, Czech Republic
Paula Louro, ISEL/IPL & CTS/UNINOVA, Portugal
Vladimir Lukin, National Aerospace University, Kharkov, Ukraine
Dandan Ma, Northwestern Polytechnical University, China
Wei Ma, The Hong Kong Polytechnic University, Hong Kong
Stephane Maag, Télécom SudParis, France
Adnan Mahmood, Macquarie University, Australia
Marco Manso, PARTICLE, Portugal
Jan Mareš, University of Chemistry and Technology, Prague, Czech Republic
Vincenzo Marletta, University of Catania, Italy
Nader Mbarek, University of Bourgogne Franche-Comté, France
Massimo Merenda, CNIT - Consorzio Nazionale Interuniversitario per le Telecomunicazioni / University Mediterranea of Reggio Calabria, Italy
Lyudmila Mihaylova, University of Sheffield, UK
Carolina Miozzi, University of Rome Tor Vergata / RADIO6ENSE srl, Italy
Olga A. Fedorova, A. N. Nesmeyanov Institute of Organoelement Compounds, Moscow, Russia
Michael Niedermayer, Berliner Hochschule für Technik (BHT), Germany
Anna Ostaszewska-Liżewska, Warsaw University of Technology, Poland
Mehmet Akif Özdemir, Izmir Katip Celebi University, Turkey
Udayan Sunil Patankar, TalTech University of Technology, Tallinn, Estonia
D. R. Patil, Rani Laxmibai Mahavidyalaya Parola | North Maharashtra University, Jalgaon, India
Pablo Pérez García, Instituto de Microelectrónica de Sevilla, Spain
Vengadesh Periasamy, Low Dimensional Materials Research Centre (LDMRC) | Institute of Ocean, Earth

and Sciences (IOES) | University of Malaya, Malaysia
Patrick Pons, CNRS-LAAS, Toulouse, France
Rüdiger Pryss, University of Würzburg, Germany
Parvaneh Rahimi, Institute of Electronic - and Sensor Materials | TU Bergakademie Freiberg, Germany
Reza Rashidi, State University of New York - Alfred State College, USA
Càndid Reig, University of Valencia, Spain
Almudena Rivadeneyra, University of Granada, Spain
Alexandra Rivero García, Universidad de La Laguna, Spain
Christos Riziotis, National Hellenic Research Foundation, Greece
Bahram Djafari Rouhani, Université de Lille Sciences et Technologies, France
Gonzalo Sad, CIFASIS / CONICET / FCEIA | Universidad Nacional de Rosario, Argentina
Markus Santoso, University of Florida, USA
Iván Santos González, Universidad de La Laguna, Spain
Jagannathan Sarangapani, Missouri University of Science and Technology, USA
Mu-Chun Su, National Central University, Taiwan
Roman Szewczyk, Warsaw University of Technology, Poland
Alessandro Tognetti, University of Pisa, Italy
Matteo Tonezzer, CNR-IMEM, Trento, Italy
Anish Chand Turlapaty, Indian Institute of Information Technology Sri City, Chittoor, India
Diego Vergara, Universidad Católica Santa Teresa De Jesús De Ávila, Spain
Sudip Vhaduri, Fordham University, USA
Manuel Vieira, CTS-ISEL, Portugal
Manuela Vieira, ISEL-IPL/CTS-UNINOVA, Portugal
Stefanos Vrochidis, Information Technologies Institute - CERTH, Greece
Guang Wang, Rutgers University, USA
Xianpeng Wang, Hainan University, China
Ulf Witkowski, South Westphalia University of Applied Sciences, Germany
Qingsong Xu, University of Macau, Macau, China
Murat Kaya Yapici, Sabanci University,Istanbul, Turkey
Sergey Yurish, Excelera, S. L. | IFSA, Spain
Lan Zhang, AIST, Japan
Jingjing Zheng, CISTER Research Centre, Portugal

Copyright Information

For your reference, this is the text governing the copyright release for material published by IARIA.

The copyright release is a transfer of publication rights, which allows IARIA and its partners to drive the dissemination of the published material. This allows IARIA to give articles increased visibility via distribution, inclusion in libraries, and arrangements for submission to indexes.

I, the undersigned, declare that the article is original, and that I represent the authors of this article in the copyright release matters. If this work has been done as work-for-hire, I have obtained all necessary clearances to execute a copyright release. I hereby irrevocably transfer exclusive copyright for this material to IARIA. I give IARIA permission or reproduce the work in any media format such as, but not limited to, print, digital, or electronic. I give IARIA permission to distribute the materials without restriction to any institutions or individuals. I give IARIA permission to submit the work for inclusion in article repositories as IARIA sees fit.

I, the undersigned, declare that to the best of my knowledge, the article is does not contain libelous or otherwise unlawful contents or invading the right of privacy or infringing on a proprietary right.

Following the copyright release, any circulated version of the article must bear the copyright notice and any header and footer information that IARIA applies to the published article.

IARIA grants royalty-free permission to the authors to disseminate the work, under the above provisions, for any academic, commercial, or industrial use. IARIA grants royalty-free permission to any individuals or institutions to make the article available electronically, online, or in print.

IARIA acknowledges that rights to any algorithm, process, procedure, apparatus, or articles of manufacture remain with the authors and their employers.

I, the undersigned, understand that IARIA will not be liable, in contract, tort (including, without limitation, negligence), pre-contract or other representations (other than fraudulent misrepresentations) or otherwise in connection with the publication of my work.

Exception to the above is made for work-for-hire performed while employed by the government. In that case, copyright to the material remains with the said government. The rightful owners (authors and government entity) grant unlimited and unrestricted permission to IARIA, IARIA's contractors, and IARIA's partners to further distribute the work.

Table of Contents

Using Machine Learning to Perform Force Calibration of Soft Triaxial Magnetic Sensors and Identify the Temperature of Grasped Objects

Yao-Wei Tian
Department of Institute of Mechatronic
Engineering of NTUT
Taipei, Taiwan
Email: t109408014@ntut.edu.tw

Jung-Tang Huang
Department of Institute of Mechatronic
Engineering of NTUT
Taipei, Taiwan
Email: jthuang@ntut.edu.tw

***Abstract*—The purpose of this research is to develop a low-cost and high-accuracy force sensor. The three-axis magnetic field change value and the surface temperature of the touch object can be obtained by using a magnet, a silicone block, and a Hall sensor. Through the self-developed automatic calibration machine and machine learning, the magnetic field value can be directly output as a three-axis force. Today's three-axis force sensors are bulky and expensive, even if the single-axis force sensors have been developed. However, it cannot provide precise tactile information like human beings, and we believe that multi-axial force perception is bound to provide more control information for robots. Therefore, this study designs a high-precision and low-cost triaxial force sensor by machine learning and an automatic calibration machine.**

Keywords- hall-sensor; Soft sensor; force and tactile sensor.

I. INTRODUCTION

In recent years, the ability of visual recognition and speech recognition has become stronger and stronger. Accurate portrait recognition and ubiquitous voice assistants have been integrated into our lives. However, the feedback of robots for touch is still insufficient [1], and cannot be like human fingers. It can accurately sense changes in the hardness, temperature, and weight of objects, so if the robot wants to grab objects that change in weight, it can usually only apply enough force. In case of plastic bottles that are filling water, excessive force can cause deformation of the bottle, so the force applied must be adjusted as the amount of water increases.

Most of the force sensors used in current automation equipment and robots are rigid materials, which are less able to withstand excessive impact and deformation [2]-[4], and sensors that can measure more than one axis are usually larger in size. Common tactile sensors, such as capacitive, optical and resistive types, have high measurement accuracy, but the disadvantage is that such sensors are relatively precise and large in size, and the disadvantages are as follows: (1) The shear force cannot be measured, (2) the scalability is poor, and (3) the temperature of the grasped object cannot be determined.

Usually, the body of the tactile sensor with higher resolution is more precise, so the expansibility will be poor, the number of circuits will be increased, and the measurement range will be sacrificed if the resolution is high. Therefore, the force sensor composed of soft materials, magnets, and Hall sensors in this study is expected to achieve the following goals: (1) Accurately measure normal force and shear force, (2) Accuracy less than 0.1N, (3) Identify temperature of touched items.

Different from the work done by Holgado et al. [5], since the sensor body is converted into the force value by the deformation of the soft material, the force can be accurately identified when the positive force is applied alone, but if the force of more than two axes is given, there will be a coupling situation, and the normal force value at this time will be affected by the lateral force, so it is difficult to accurately derive it with a general calculation formula. We collect data from our self-developed auto-calibration platform and use Neural Network and Recurrent Neural Network to convert sensor data to force.

In order to obtain a more anthropomorphic touch, we will identify the temperature of the object touched by the sensor, so that the mechanical gripper or other applications equipped with this sensor can obtain more sensing information.

II. SENSOR ARCHITECTURE

The main body of the sensor is shown in Fig.1, which includes a silicone block, a magnet, and a flexible circuit board. The Hall sensor MLX90393 is used on a 13 mm * 13 mm flexible circuit board to read the three-axis magnetic flux. The communication between the sensor and the host computer uses I2C to communicate because it can share a common data bus with more sensors to save wiring space.

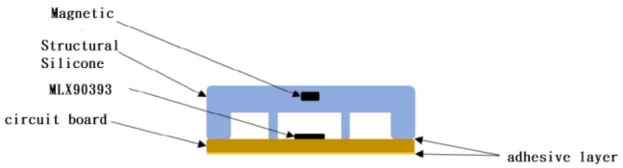

Figure 1. Sensor Schematic.

A. Flexible circuit board

Since the sensor body is composed of a silicone block, a magnet, and a sensor chip, and communicates through I2C, the circuit and wiring can be simplified, and the values of all sensors can be connected in series through a bus, and the assembly. When it is installed on the gripper, it can reduce the wiring on the equipment, and the host computer is also more convenient for control.

B. Silicone structure

The silicone structure uses TSE 221-4U, the specifications are shown in the Table I, a ø2*1mm N35 axial magnet is embedded in the center of the structure, as shown in Fig.2, a hole is designed in the silicone layer to accommodate the magnet, and ensure that the magnet is not under stress directly above the sensing wafer. TSE 221-4U silicone is suitable in the range of 30(N) in our designed structure.

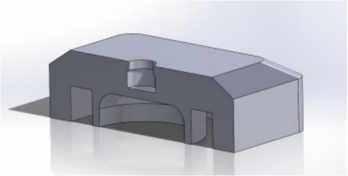

Figure 2. Silicone structure Schematic.

TABLE I. SILICONE RUBBER TYPICAL PROPERTY DATA

Specification	***TSE221-4U***	***unit***
Density	1.13	g/cm^3
Hardness	40	°A
Tensile strength	8.4	MPa
Tear strength	23	N/mm
Elongation	500	%
Compression set	19	%

C. Magnetic

For the selection of magnets, we evaluated two types of magnets, N35 and N50, and observed the relationship between the magnetic field strengths of the magnets and the sensing chip at different positions. As shown in the Fig.3, when the N50 magnet is close to 1 mm or less, the measurement of the magnetic field is almost saturated, and the sensing range is also reduced. Therefore, the N35 magnet is used to make the sensor.

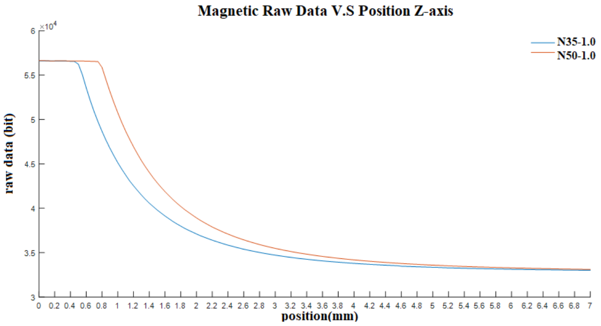

Figure 3. The relationship between the magnetic field and the position of the N35 and N50 magnets

III. AUTOMATIC CALIBRATION MACHINE

In order to identify the relationship between the real force and the magnetic field, we design an automatic calibration machine, which can perform force calibration in three axes. As shown in the Fig.4, using stepper motors, linear slides, and six-axis force-torque sensors, high-precision position and force control can be performed, and tactile sensors can be verified and analyzed.

The six-axis force and torque sensor use ATI Force/Torque Sensor Axia80-M20, which can measure the maximum 900(N) normal force and 500(N) lateral force with an accuracy of 0.1(N). Therefore, the 3D forces value and the magnitude of the magnetic field change can be obtained by using this automatic calibration machine and then the magnetic field can be converted into 3D forces through subsequent processing.

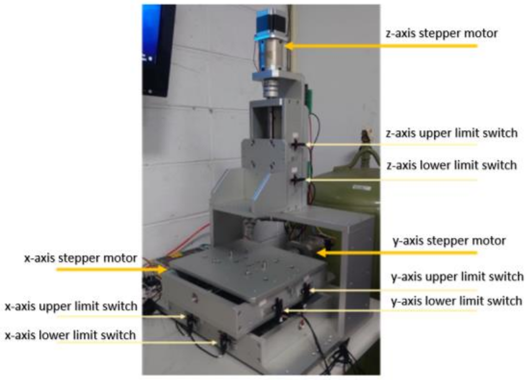

Figure 4. Automatic calibration machine

IV. MACHINE LEARNING MODELS

In recent years, the application of machine learning has developed vigorously. The most common ones are image recognition, speech recognition, and various applications. At present, most people use the Deep Neural Networks (DNN), Convolutional Neural Networks (CNN), Recurrent Neural Networks (RNN), which can analyze and calculate many tasks with such neural network models, among which we found that neural network models related to time series are more suitable for use in calibrating sensor models. So we try to use this for sensor development.

Through the test of the sensor by the automatic calibration machine, we can obtain the original data of the sensor corresponding to the real 3D forces. When the normal force is applied alone, the accuracy is about 0.1 (N), but because of the relationship of the silicone structure, the multi-axis force will cause the signals to couple with each other, and it is difficult to calculate the relationship using general mathematical formulas. Therefore, we have tried a neural network model and a time series model to convert data and power, and use this method to distinguish the two relationships between them.

A. Data format

During calibration, we use the Arduino Uno board as the host computer of the sensor and use the serial port monitoring window to read the sensor's three-axis data and temperature values (R_x, R_y, R_z, T). The automatic calibration machine obtains three-axis force values (F_x, F_y, F_z). Through the above data, our sensor data R_i is the input, and the force value F_i is the output. The temperature value does not need to be used since it does not need to be calibrated.

B. Data processing

The initial value of the sensor is read in before training, and we set the maximum value of the data to 57000 bits and normalize it. The collected initial data (input_min) and the upper limit data (input_max) are used as the maximum and minimum values of the formula. When performing calibration in the future, the initial state also needs to be read as the initial value of the sensor. Its purpose is to reduce the situation that the results will fail to converge during training.

C. Neural Networks force fitting model

Using machine learning to convert between magnetic field and force, we designed a four-layer model architecture, as shown in the Fig.5, using functions such as ReLU, Tanh, Linear, and BatchNorm1d, and each function has 500 neurons. This is the best model architecture we have tried so far.

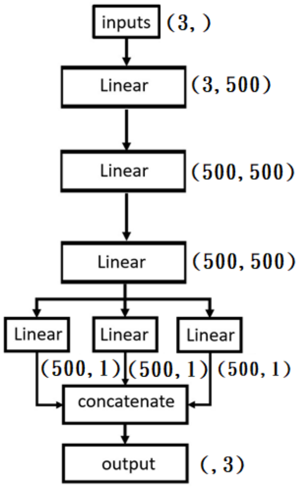

Figure 5. Neural Networks Model Architecture

D. Transformer force fitting model

Compared with neural networks, Transformer is a time series model (Sequence to Sequence model), which is similar to Recurrent Neural Networks (RNN), but RNN adopts a sequential structure, while Transformer adopts parallel training, which can make full use of all signal.

The special feature is the self-attention [6]. When we input three elements, the self-attention can simultaneously perform operations on these three elements related to each other. As shown in the Fig.6, the three axes of the sensor itself are affected by the silicone, and the three will be related to each other when the force is applied, so we think that using the Transformer will be very suitable for this project.

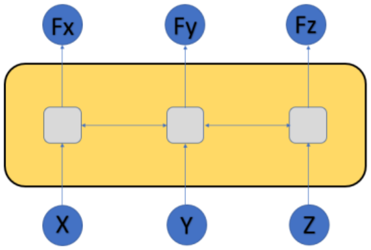

Figure 6. self-attention diagram

The data processing type is originally a two-dimensional matrix, but the time series model training must take into account the before and after the status of each data, so we will first reshape the data into a three-dimensional matrix. Each piece of data is the current data and the next 30 pieces of data as a unit for training.

The model architecture is designed with two layers. The first layer is the Transformer layer, including functions such as ReLU and Linear. The second layer uses functions such as ReLU, Tanh, Linear, and BatchNorm1d, and each layer is calculated by 64 neurons.

V. EXPERIMENT

From the reading value of the sensor to the pressure value, we divide the system structure into 5 layers, as shown in the Fig.7, from top to bottom are data reading, data processing, and power conversion. For the power conversion part, we use an automatic calibration machine to calibrate and store the data into the machine learning model for training.

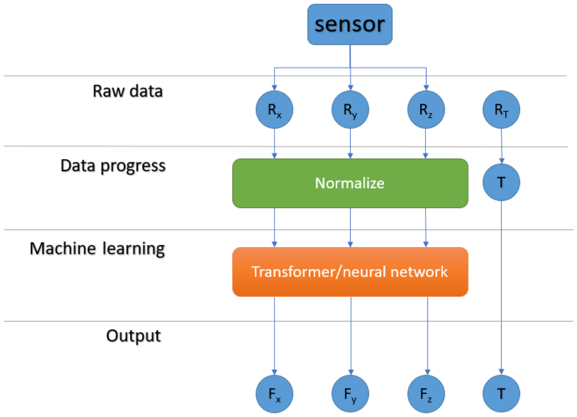

Figure 7. System Architecture Diagram

A. *Temperature recognition*

When we touch different objects, we can identify their temperature by the conduction of thermal energy. We use a heat gun to heat the sensor and use an infrared thermal imager as the ground truth of the thermal energy. As shown in Fig.8, when it is not heated, the ambient temperature is about 26 degrees C. After heating, we increase the temperature to 30 degrees C and identify its temperature value.

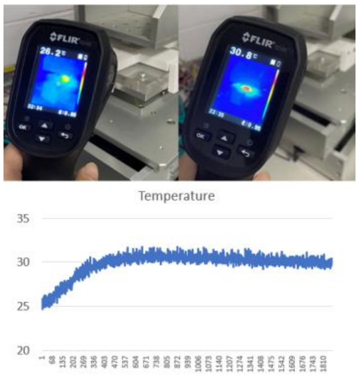

Figure 8. Comparison of sensor heating temperature and infrared thermal imager

B. *Sensor Calibration*

In order to convert the sensor data, we obtain the real pressure value through automatic machine calibration, and apply more than two axes of force for grasping objects. As shown in Fig.9, the first is the normal force applied to the object, and the second and third are the shear forces parallel to the sensor against gravity. Therefore, the calibration is also divided into two types: normal force correction and shear force correction. We record 5000 pieces of data every 5(N) for the sensor and record 7 groups from 0 to 30(N). The second part applies the lateral force of the X-axis for every 5(N) of the normal force, the third part applies a Y-axis lateral force for every 5(N) of the normal force.

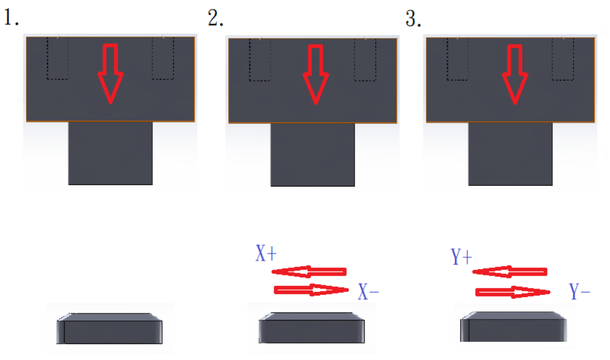

Figure 9. Sensor Calibration Diagram

As shown in Fig.10, a normal force of 10 (N) is applied. We can find that the accuracy of the automatic calibration machine is 0.1 (N). The actual measurement result increases with the increase of the normal force, and the sheer force also increases. By applying positive and negative X-axis shear force, you can see that the X-axis force value of the automatic calibration machine will follow the fluctuation. We repeat this method to collect normal force and shear force data, and then throw them into the neural network model training.

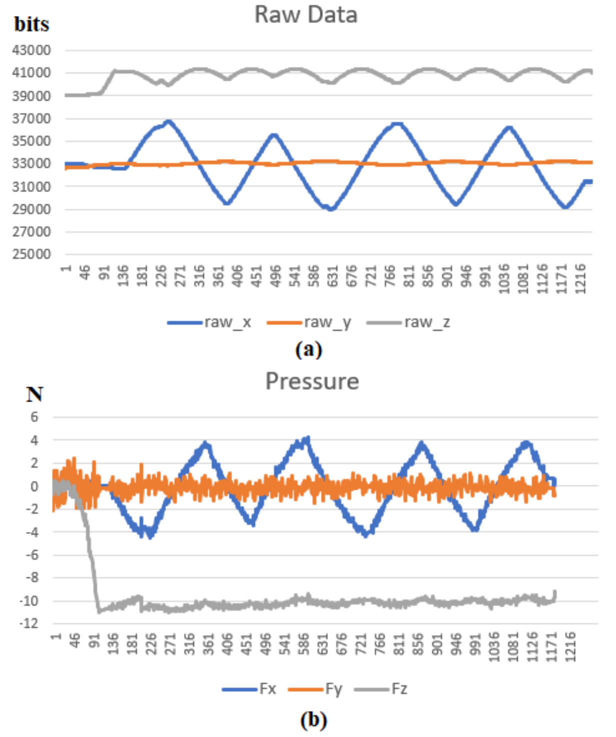

Figure 10. Sensor and calibration platform 10N force value(a) Magnetic force raw data measured by the sensor.(b) Triaxial force measured by automatic calibration machine.

C. *Neural Network and Transformer comparison*

In the first experiment, we use an automatic calibration machine to simulate grasping an object. As shown in Fig.11, a positive force and a gradually increasing lateral force will be applied at this time, and the middle will gradually increase by 1(N), so that the force of the Y-axis will gradually increase, and the positive force will be constant.

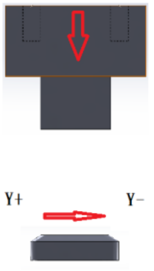

Figure 11. Automatic calibration machine pressure test chart

As shown in Fig.12, the vertical axis is the force value N, and the horizontal axis is the number of data strokes. We apply a normal force of 15(N) and gradually increase the force on the Y axis, the target is the ground truth, and pred is the force value predicted by the model. It can be seen that the results calculated by the model generally follow the trend of the real data. We use the same data to compare the differences between the two models. As shown in Table II, we compared the root mean square error and absolute value average error between the two models, and the difference in root mean square error is 1.06 (N), so it can be seen that using Transformer does get better results.

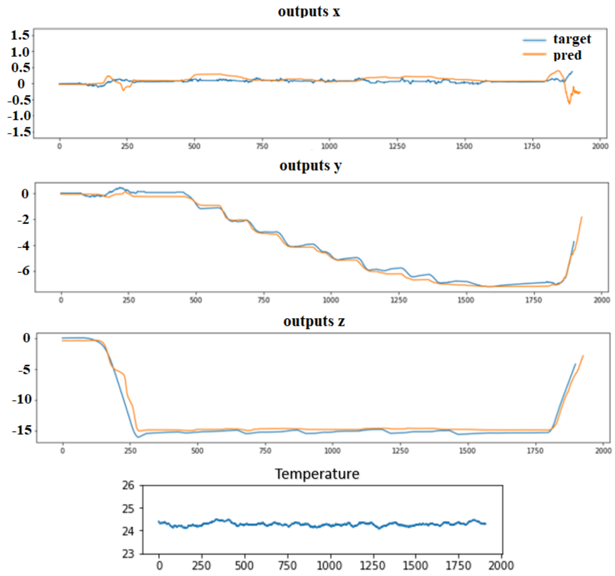

Figure 12. Three-axis force ground truth (target), force prediction value (pred)) and measured temperature value

TABLE II. NEURAL NETWORKS AND TRANSFORMER WITH OR WITHOUT TEMPERATURE COMPENSATED RMSE AND MAE

type	*RMSE*	*MAE*
NN	1.39	1.1
Transformer	0.33	0.22

D. Temperature Identification Test

This experiment is to place a water glass above the sensor and gradually add hot water to measure the temperature change while sensing the normal force. In the process, we first put a mug on the pressure and shear force sensor, and then gradually pour hot water. The temperature part is verified by an infrared thermal imager. The weight of the mug is 3.4 (N), and 180 ml of hot water at 50 degrees C is equivalent to 1.8 (N). As shown in Fig.13, in section 1, the weight of 3.4(N) is measured after placing the mug.

In section 2, the weight change gradually increases by 1.9(N) after adding hot water, and in section 3 is the shaking during the experiment. As a result, the fourth section is placed above the sensor stably, and the measured total weight is 5.31(N). As shown in Fig.14, the temperature of the cup was measured to be about 23 degrees C when the hot water was not poured, and the temperature of the cup rose to 37.1 degrees C after the hot water was poured. The temperature measured at the bottom of the cup is about 26.2 degrees C. In the graph of pressure and temperature change in Fig.13, it can be seen that the sensor can accurately measure the temperature of the bottom of the cup and the change in the weight of the item..

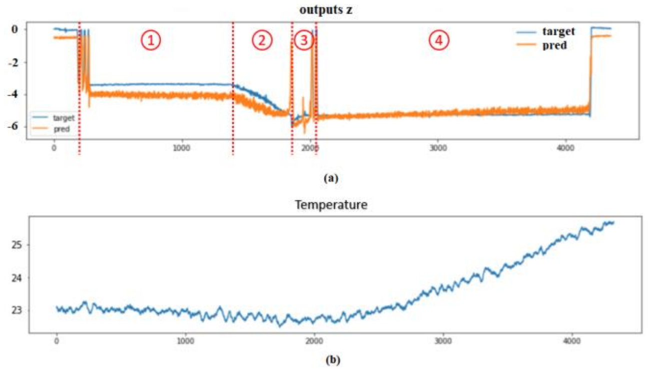

Figure 13. Normal force measurement and temperature measurement diagram: (a) normal force actual force curve and force prediction curve, (b) 3D force sensor surface temperature diagram

Figure 14. Infrared thermal imager temperature change

VI. CONCLUSION

This research was to design a tactile sensor, which could make the device have skin like the human body, and could know the weight and temperature of the object. We also used machine learning and a calibration machine to calculate the precise force value. Therefore, the tactile sensor designed in this research will be able to be used in the robot as a feedback signal for precise force control.

At present, the accuracy of the automatic calibration machine may not be high enough, so the corrected error was relatively large, and we continued to improve the machine learning model, hoping to reduce its error and consider the hysteresis of the sensor itself. Since the contact surface of the sensor body was a silicone structure, the heat conduction will be slightly delayed when sensing the temperature of the object. Therefore, in the future, graphite powder will be mixed into the silicone structure to increase the heat conduction speed, and the measured temperature value will be higher and more precise without long delay time.

In the future, we hope to design a sensor that can recognize the position of multiple points on this sensing surface, and improve the application range of 3D force. The application of multi-point recognition can improve the recognition of the outline of the grasped object, so it can provide more accurate information for robots with real tactile feedback.

REFERENCES

[1] R. Bhirangi, T. Hellebrekers, "ReSkin: versatile, replaceable, lasting tactile skins ", 5th Conference on Robot Learning (CoRL 2021), London, UK, 2021, pp. 1.

[2] W. H. Ko and Q. Wang, "Touch mode capacitive pressure sensors," Sensors and Actuators A: Physical, vol. 75, no. 3, 1999, pp. 242-251.

[3] S. Guo, J. Guo, and W. H. Ko, "A monolithically integrated surface micromachined touch mode capacitive pressure sensor," Sensors and Actuators A: Physical, vol. 80, no. 3, 2000, pp. 224-232.

[4] E. Hwang and Y. Kim, "A Polymer-based Flexible Tactile Sensor and Its Application to Robotics," in SENSORS, 2007, pp. 784-787.

[5] A C. Holgado, N. Piga, T P Tomo, G Vezzani, A. Schmitz, L. Natale, S. Sugano, "Magnetic 3-axis Soft and Sensitive Fingertip Sensors Integration for the iCub Humanoid Robot", IEEE Robotics and Automation Letters, VOL. 5, NO. 3, JULY 2020, pp. 2-3.

[6] A. Vaswani, N. Shazeer, N. Parmar, J. Uszkoreit, L. Jones, A. N. Gomez, L. Kaiser, I. Polosukhin," Attention Is All You Need" 31st Conference Neural Information Processing Systems, 2017, pp. 2-8.

Indoor Guidance Services through Visible Light Communication

Manuela Vieira, Manuel Augusto Vieira, Paula Louro, Alessandro Fantoni
ADETC/ISEL/IPL,
R. Conselheiro Emídio Navarro, 1959-007
Lisboa, Portugal
CTS-UNINOVA
Quinta da Torre, Monte da Caparica, 2829-516,
Caparica, Portugal

e-mail: mv@isel.ipl.pt, mv@isel.pt, plouro@deetc.isel.pt,
afantoni@deetc.isel.ipl.pt

Pedro Vieira
ADETC/ISEL/IPL,
R. Conselheiro Emídio Navarro, 1959-007
Lisboa, Portugal
Instituto das Telecomunicações
Instituto Superior Técnico, 1049-001,
Lisboa, Portugal
e-mail: pvieira@isel.pt

Abstract— Communications within personal working/living spaces are highly demanded. To support people's wayfinding activities, we propose a Visible Light Communication (VLC) cooperative system that supports guidance services and uses an edge/fog-based architecture for wayfinding services. A mesh cellular hybrid structure is proposed. The dynamic navigation system is composed of several transmitters (ceiling luminaries), which send the map information and path messages required to wayfinding. The luminaires are equipped with one of two types of nodes: a "mesh" controller that connects with other nodes in its vicinity and can forward messages to other devices in the mesh, effectively acting like routers nodes in the network and a "mesh/cellular" hybrid controller, that is also equipped with a modem providing IP base connectivity to the central manager services. These nodes act as border-router and can be used for edge computing. Mobile optical receivers, using joint transmission, collect the data at high frame rates, extracts their location to perform positioning and, concomitantly, the transmitted data from each transmitter. Each luminaire, through VLC, reports its geographic position and specific information to the users, making it available for whatever use. Bidirectional communication is implemented and the best route to navigate through venue calculated. The results show that the system makes possible not only the self-localization, but also to infer the travel direction and to interact with information received optimizing the route towards a static or dynamic destination.
.

Keywords- Visible Light Communication; Indoor navigation; Bidirectional Communication; Wayfinding, Optical sensors; Indoor multi-level environments; Transmitter/Receiver.

I. INTRODUCTION

Nowadays, wireless networks have seen a demand for increased data rate requirements. For a realistic coverage with the data rate requirements, a large bandwidth is needed which remains a limiting factor when compared with the RF communication technologies. Consequently, research has started exploring alternate wireless transmission technologies to meet the ever-increasing demand. In this context, the huge bandwidth available in the unlicensed electromagnetic spectrum in the optical domain is seen as a promising solution to the spectrum crunch.

Visible Light Communication (VLC) makes use of the higher frequencies in the visual band and extends the capabilities of data transmission using general light sources. VLC has been regarded as an additional communication technology [1] [2] to fulfill the high data rate demands and as a new affiliate in the beyond fifth generation (5G) heterogeneous networks. It can be easily used in indoor environments using the existing LED lighting infrastructure with few modifications [3] [4]. Research has shown that compared to outdoors, people tend to lose orientation a lot easier within complex buildings [5] [6]. Fine-grained indoor localization can be useful, enabling several applications [7] [8].

This work focuses on the use of VLC as a support for the transmission of information, providing advertising services and specific information to users. The goal is a cooperative system that supports guidance services and uses an edge/fog based architecture for wayfinding services. Here, the luminaire, through VLC, reports its geographical positions and specific information to the users since its infrastructure can also be reused to embed the fog nodes in them. The system is composed of several transmitters (LEDs luminaries), which send the map information and path messages required to wayfinding. Data is encoded, modulated and converted into light signals emitted by the transmitters. Every mobile terminal is equipped with a receiver module for receiving the mapped information generated from the ceiling light and displays this information in the mobile terminal. The receiver module includes a photodetector based on a tandem a-SiC:H/a-Si:H pin/pin light-controlled filter [9] [10].

Visible light can be used as an ID system and can be employed for identifying the room number and the building itself. The main idea is to divide the service area into spatial beams originating from the different ID light sources and identify each beam with a unique timed sequence of light signals. The signboards, based on arrays of LEDs, positioned in strategic directions to broadcast the information [11], are modulated acting as down- and up-link channels in the bidirectional communication. For the consumer services, the applications are enormous. The objective is to allow the implementation of new services in these areas using data from the VLC System, for indoor and outdoor. Positioning, navigation, security and even mission critical services are possible use cases that should be implemented.

In this paper, a LED-supported guidance VLC system is proposed. After the Introduction, in Section II, the communication system is described. In Section III, the main experimental results are presented, downlink and uplink transmission is implemented and the best route to navigate calculated. In Section IV, the conclusions are drawn.

II. COMMUNICATION SYSTEM, DESIGN AND ARCHITECTURE

The main goal is to specify the system conceptual design and define a set of use cases for a VLC based guidance system to be used by mobile users inside large buildings.

A. *Communication system and cooperative localization*

The system is composed by two modules: the transmitter and the receiver. The block diagram and the transmitter and receiver relative positions are presented in Figure 1. Both communication modules are software defined, where modulation/ demodulation can be programed

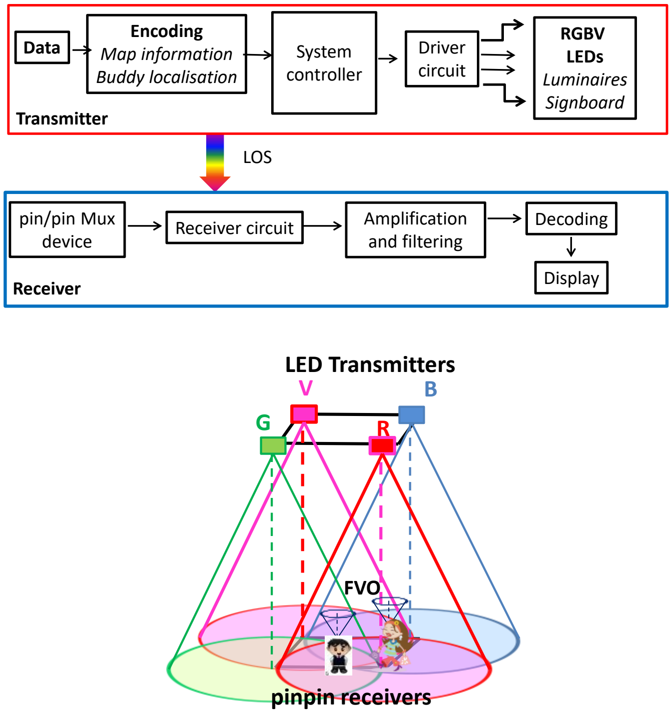

Figure 1. Block diagram and transmitters and receivers 3D relative positions.

Data from the sender is converted into an intermediate data representation, byte format, and converted into light signals emitted by the transmitter module. The data bit stream is input to a modulator where an ON–OFF Keying (OOK) modulation is utilized. On the transmission side, a modulation and conversion from digital to analog data is done. The driver circuit will keep an average value (DC power level) for illumination, combining it with the analog data intended for communication. The visible light emitted by the LEDs passes through the transmission medium and is then received by the MUX device.

To realize both the communication and the building illumination, white light tetra-chromatic sources are used providing a different data channel for each chip. Each luminaire is composed of four white LEDs framed at the corners of a square. At each node, only one chip of the LED is modulated for data transmission, the Red (R: 626 nm), the Green (G: 530 nm), the Blue (B: 470 nm) or the Violet (V). Data is encoded, modulated and converted into light signals emitted by the transmitters. Modulation and digital-to-analog conversion of the information bits is done using signal processing techniques. The signal is propagating through the optical channel and a VLC receiver, at the reception end of the communication link, is responsible to extract the data from the modulated light beam. It transforms the light signal into an electrical signal that is subsequently decoded to extract the transmitted information.

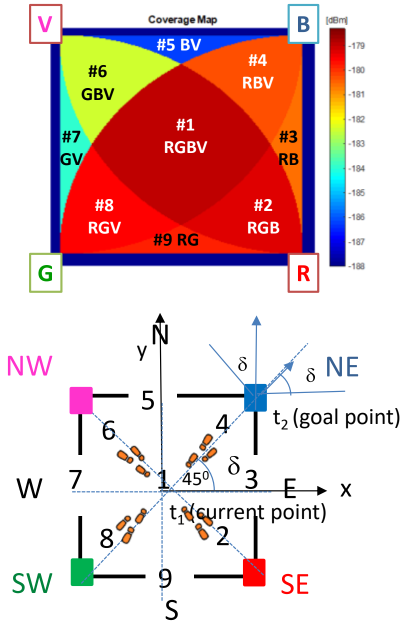

Figure 2. Illustration of the coverage map in the unit cell: footprint regions (#1-#9) and steering angle codes (2-9).

On the receiving side, this is first done by a silicon carbide (SiC) pinpin MUX device that acts as an active filter for the visible region of the light spectrum. After receiving the signal, it is in turn filtered, amplified, and converted back to digital format for demodulation. The system controller consists of a set of programmable modules. To receive the I2V information from several transmitters, the receiver must be located at the overlap of the circles that set the transmission range (radial) of each transmitter. The coverage map for a square unit cell is displayed in Figure 2. The LEDs are modeled as Lambertian sources where the luminance is distributed uniformly in all directions, whereas the luminous intensity is different in all directions [12]. The nine possible overlaps (#1-#9), defined as fingerprint regions, as well as receiver orientations (2-9 steering angles; δ) are also pointed out for the unit square cell in Figure 2. The input of the aided navigation system is the coded signal sent by the transmitters to an identify user, and includes its position in the network $P(x, y, z)$, inside the unit cell and the steering angle, δ, that guides the user across his path. The device receives multiple signals, finds the centroid of the received coordinates, and stores it as the reference point position. Nine reference points, for each unit cell, are identified giving a fine-grained resolution in the localization of the mobile device across each cell.

The VLC photosensitive receiver is a double pin/pin photodetector based on a tandem heterostructure, p-i'-n/p-i-n sandwiched between two conductive transparent contacts. Exposed to light, the device offers high sensitivity and linear response, generating a proportional electrical current. Its quick response enables the possibility of high-speed communications. Since the photodetector response is insensitive to the frequency, phase, or polarization of the carriers, this kind of receiver is useful for intensity-modulated signals. The generated photocurrent is processed using a transimpedance circuit obtaining a proportional voltage. An OOK modulation scheme was used to code the information. This way digital data is represented by the presence or absence of a carrier wave. The obtained voltage is then processed, by using signal conditioning techniques (adaptive bandpass filtering and amplification, triggering and demultiplexing), until the data signal is reconstructed at the data processing unit (digital conversion, decoding and decision) [13] [14].

B. *Architecture and Multi-person Cooperative Localization*

Fog/Edge computing bridges the gap between the cloud and end devices by enabling computing, storage, networking, and data management on network nodes within the close vicinity of IoT devices. A mesh network is a good fit since it dynamically reconfigures itself and grows with the size of any installation. In Figure 3, the proposed architecture is illustrated.

Under this architecture, the short-range mesh network purpose is twofold: enable edge computing and device-to-cloud communication, by ensuring a secure communication from a luminaire controller to the edge computer or datacenter (I2CM), through a neighbor luminaire/signboard controller with an active cellular connection; and enable peer-to-peer communication (I2I), to exchange information. It performs much of the processing on embedded computing platforms, directly interfacing to sensors and controllers. It supports geo-distribution, local decision making, and real-time load-balancing. Moreover, it depends on the collaboration of near-located end-user devices, instead of relying on the remote servers, which reduces the deployment costs and delay.

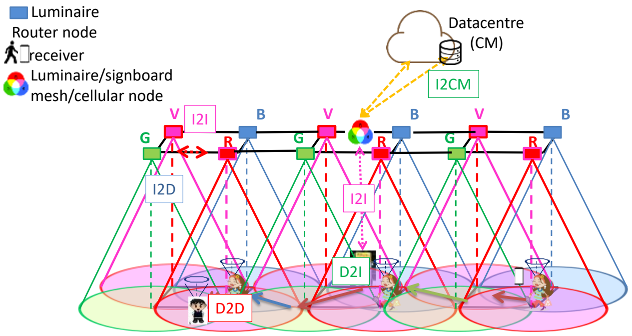

Figure 3. Mesh and cellular hybrid architecture.

C. *Scenario and building model*

Building a geometry model of buildings' interiors is complex. In the proposed architecture each room/crossing/exit represents a node, and a path as the links between nodes. The proposed scenario is a multi-level building. Lighting in large environments is designed to illuminate the entire space in a uniform way. Ceiling plans for the LED array layout, in floor level is shown in Figure 4.

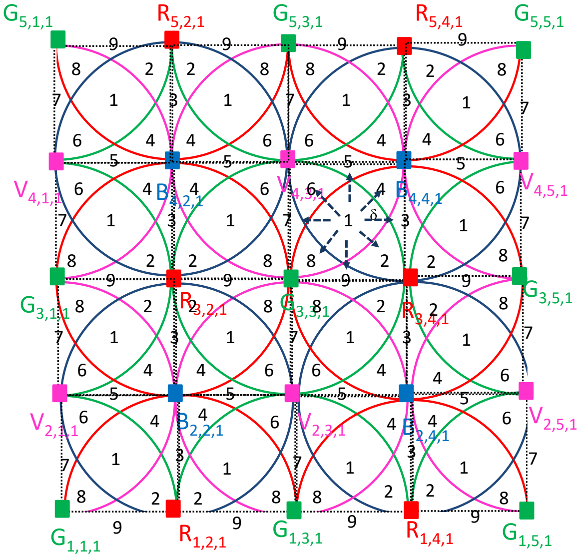

Figure 4. Illustration of the optical scenarios (RGBV =modulated LEDs spots). Clusters of cells in square topology.

A square lattice topology was considered for each level. A user navigates from outdoor to indoor. It sends a request message to find the right track (D2I, in Figure 3) and, in the available time, he adds customized points of interest (wayfinding services). The requested information (I2D) is sent by the emitters at the ceiling to its receiver.

The indoor route throughout the building (track) is presented to the user by a responding message transmitted by the ceiling luminaires that work also either as router or mesh/cellular nodes. With this request/response concept, the generated landmark-based instructions help the user to unambiguously identify the correct decision point where a change of direction (pose) is needed, as well as offer information for the user to confirm that he/she is on the right way.

III. GEOTRACKING, NAVIGATION AND ROUTE CONTROL

Bi-directional communication between the infrastructure and the mobile receiver is analyzed.

A. Communication protocol and coding/decoding techniques

To code the information, an On-Off Keying (OOK) modulation scheme was used, and it was considered a synchronous transmission based on a 64- bits data frame.

The frame is divided into six blocks (Sync, ID, pin1/pin2, Angle δ, Request/Response and Wayfinding Data). The first block is the synchronization block [10101], the last is the payload data (wayfinding message) and a stop bit ends the frame. The second block, the ID block, 4+4+4 bits, gives the geolocation (*x*,*y*,*z* coordinates) of the emitters inside the array ($X_{i,j,k}$). Cell's IDs are encoded using a 4 bits binary representation for the decimal number. When bidirectional communication is required, the user must register by choosing a username (pin_1) with 4 decimal numbers, each one associated to a RGBV channel. If buddy friend services are required a 4-binary code of the meeting (pin_2) must be inserted. The δ block (steering angle (δ)) completes the pose in a frame time q(x,y, δ, t). Eight steering angles along the cardinal points are possible from a start point to the next goal as pointed out as dotted arrows in Figure 4. The codes assigned to the pin_2 and to δ are the same in all the channels. If no wayfinding services are required these last three blocks are set at zero and the user only receives its own location. The last block is used to transmit the wayfinding message.

When bidirectional communication is required, the user must register by choosing a username (pin_1) with 4 decimal numbers, each one associated to a colour channel. So, to compose the decimal code each digit (0-9) has its own colour, codified in a 4-binary bit code. If buddy friend services are required a 4-binary code of the meeting (pin_2) must be inserted. The δ block (steering angle (δ)) completes the pose in a frame time q(x,y, δ, t). Eight steering angles along the cardinal points and coded with the same number of the footprints in the unit cell (Figure 2) are possible from a start point to the next goal. If no wayfinding services are required these last three blocks are set at zero and the user only receives its own location. The last block is used to transmit the wayfinding message. A stop bit is used at the end of each frame.

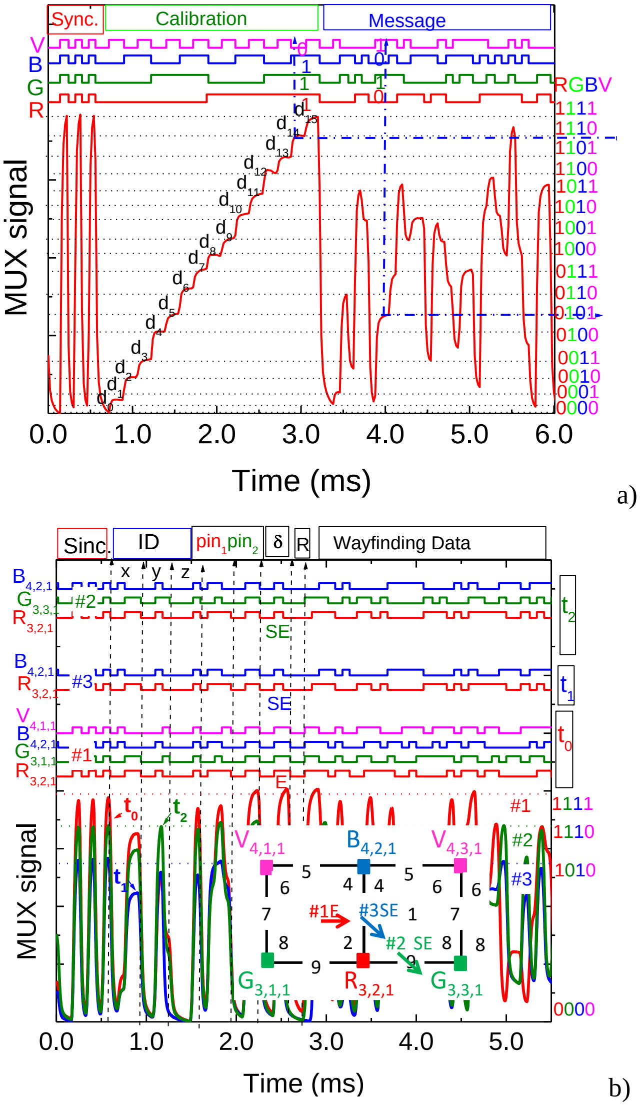

a)

b)

Figure 5. a) MUX/DEMUX signals of the calibrated cell. In the same frame of time a random signal (Message) is superimposed. b) Fine-grained indoor localization and navigation in successive instants. On the top the transmitted channels packets are decoded [R, G, B, V].

Based on the measured photocurrent signal by the photodetector, it is necessary to decode the information received. A calibration curve is previously defined to establish this assignment. In Figure 5a, it is plotted the calibration curve that uses 16 distinct photocurrent thresholds resultant from the combination of the RGBV modulated signals from VLC emitter. The correspondence between each 4-binary code and the photocurrent level is highlighted on the right side. Here, the MUX signal obtained at the receiver as well as the coded transmitted optical signals is displayed. The message, in the frame, start with the header labelled as Sync, a block of 5 bits. The same synchronization header [10101] is imposed simultaneously to all emitters. In the second block, labelled as calibration, the bit sequence was chosen to allow all the *on/off* sixteen possible combinations of the four RGBV input channels (2^4). Finally, a random message was transmitted [15]. Comparing the calibrated levels (d_0-d_{15}) with the different assigned 4-digit binary [RGBV] codes, ascribed to each level, the decoding is straightforward, and the message decoded [16].

In Figure 5b, the MUX received signal and the decoding information that allows the VLC geotracking and guidance in successive instants (t_0, t_1, t_2) from user "7261" guiding him along his track is exemplified. The visualized cells, paths, and the reference points (footprints) are also shown as inserts. Data shows that at t_0 the network location of the received signals is $R_{3,2,1}$, $G_{3,1,1}$, $B_{4,2,1}$ and $V_{4,1,1}$, at t_1 the user receives the signal only from the $R_{3,2,1}$, $B_{4,2,1}$ nodes and at t_2 he was moved to the next cell since the node $G_{3,1,1}$ was added at the receiver. Hence, the mobile user "7261" begins his route into position #1 (t_0) and wants to be directed to his goal position, in the next cell (# 9). During the route the navigator is guided to E (code 3) and, at t_1, steers to SE (code 2), cross footprint #2 (t_3) and arrives to #9. The ceiling lamps (landmarks) spread over all the building and act as edge/fog nodes in the network, providing well-structured paths that maintain a navigator's orientation with respect to both the next landmark along the path and the distance to the eventual destination. Also, the VLC dynamic system enables cooperative and oppositional geolocation. In some cases, it is in the user's interest to be accurately located, so that they can be offered information relevant to their location and orientation (pin $_1$, pin$_2$ and δ blocks). In other cases, users prefer not to disclose their location for privacy, in this case these last three blocks are set at zero and the user only receives its own location.

B. *Multi-person cooperative localization and guidance services*

Bi-directional communication between VLC emitters and receivers is available at a VLC ready handheld device, through the control manager interconnected with a signboard receiver located at each unit cells (#1). These communications channels constitute the uplink (D2I) and downlink channels (I2D). Each user (D2I) sends to the local controller a "request" message with the pose, $q_i(t)$, (x,y,z, δ), user code (pin$_1$) and also adds its needs (code meeting and wayfinding data). For route coordination the CM, using the information of the network's VLC location capability, sends a personalized "response" message to each client at the requested pose with his wayfinding needs.

In Figure 6, the MUX synchronized signals received by two users that have requested wayfinding services, at different times, are displayed. We have assumed that a user located at $C_{2,3,-1}$, arrived first (t_1), auto-identified as ("7261") and informed the controller of his intention to find a friend for a previously scheduled meeting (code 3). A buddy list is then generated and will include all the users who have the same meeting code. User "3009" arrives later (t_3), sends the alert notification ($C_{4,4,1}$; t_3) to be triggered when his friend is in his floor vicinity, level 1, identifies himself ("3009") and uses the same code (code 3), to track the best way to his meeting.

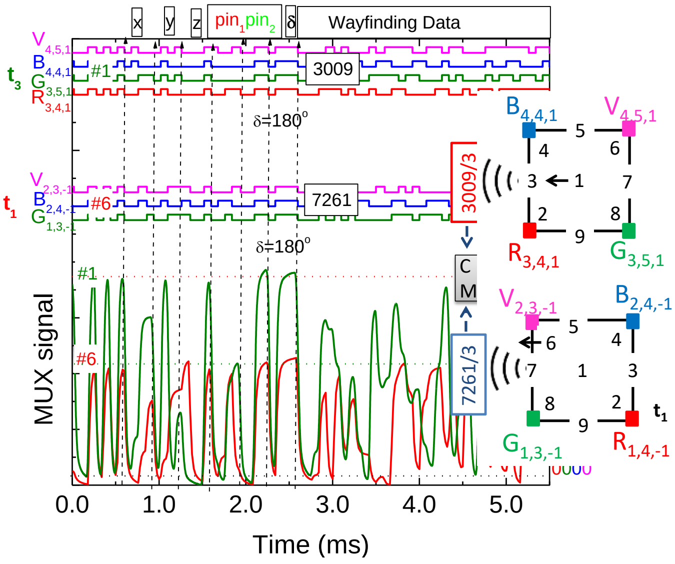

Figure 6. MUX/DEMUX signals assigned requests from two users ("3009" and "7261") at different poses ($C_{4,4,,1}$; #1W and $C_{2,3,-1}$; #6 W) and in successive instants (t_1 and t_3).

After this request (t_3), the buddy finder service uses the location information from both user' devices to determine the proximity of their owners ($q_{ij}(t)$) and sends a response message with the best route to the meeting.

The pedestrian movement along the path can be thought as a queue, where the pedestrians arrive at a path, wait if the path is congested and then move once the congestion reduces.

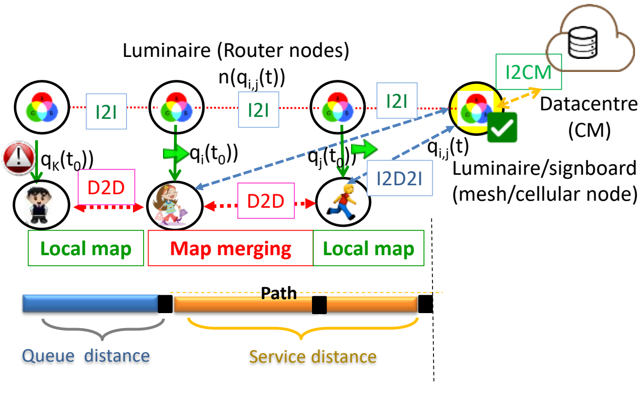

Figure 7 Graphical representation of the simultaneous localization and mapping problem using connectivity as a function of node density, mobility and transmission range.

In Figure 7, a graphical representation of the simultaneous localization and mapping problem using connectivity as a function of node density, mobility and transmission range is illustrated. The following parameters are therefore needed to model the queuing system: The initial arrival time (t_0) and the path, respectively, defined as the time when the pedestrian leaves the previous path and the actual movement along the path, $q_i (t, t')$. Here, the service time is calculated using walking speed and distance of the path. The number of service units or resources is determined from the capacity of the path, $n(q_i (x,y,z, \delta, t))$ and walking speed that depends on the number of request services, and on the direction of movement along the path $q_i (x,y,z, \delta, t)$. Since the number of service units is same as the capacity of the path, the queue size is theoretically zero. Once appended by the CM (request message), the pedestrians are served immediately (response message). If the number of pedestrians exceeds the path capacity, a backlog is automatically formed until the starting node. The hybrid controller integrates the number of requests and individual positions received during the same time interval. Once the individual positions are known, $q_i (t)$, the relative positions are calculated, $q_{ij} (t)$. If the relative position is less than a threshold distance, a crowded region locally exists, and an alert message is sent for the users. This alert allows the CM to recalculate, in real time, the best route for the users, $q_i (t,t')$, that request wayfinding services avoiding crowded regions.

IV. CONCLUSIONS

A cooperative indoor VLC localization and navigation system is proposed. In a multi-level building scenario, the architecture of the system and the protocol of communication were defined. Bi-directional communication between the infrastructure and the mobile receiver was analyzed. According to global results, the location of a mobile receiver is found in conjunction with data transmission. VLC's dynamic LED-aided navigation system is designed to give users accurate route guidance and enable navigation and geotracking. The multi-person cooperative localization system detects crowded regions and alerts the user to reschedule meetups, as well as provides guidance information. With those alerts, the CM can recalculate, in real time, the best route for users requesting wayfinding services, avoiding crowded areas.

ACKNOWLEDGEMENTS

This work was sponsored by FCT – Fundação para a Ciência e a Tecnologia, within the Research Unit CTS – Center of Technology and Systems, reference UIDB/00066/2020.

REFERENCES

[1] E. Ozgur E. Dinc, and O. B. Akan, "Communicate to illuminate: State-of-the-art and research challenges for visible light communications," Physical Communication 17 pp. 72–85, 2015.

[2] C. Yang and H. R. Shao,, "WiFi-based indoor positioning," IEEE Commun. Mag., vol. 53, no. 3, pp. 150–157, Mar. 2015.

[3] D. Tsonev, et al. "A 3-Gb/s single-LED OFDM-based wireless VLC link using a Gallium Nitride μLED," IEEE Photon. Technol. Lett. 26 (7), pp.637–640, 2014.

[4] D. O'Brien, et al., "Indoor visible light communications: challenges and prospects," Proc. SPIE 7091, 709106, pp. 60-68, 2008.

[5] H.-H. Liu and Y.-N Yang,"WiFi-based indoor positioning for multi-floor environment," Proceedings of the IEEE Region 10 Conference on Trends and Development in Converging Technology Towards (TENCON '11)November 2011Bali,Indonesia59760110.1109/TENCON.2011.61291752-s2.0-84863014825, pp.597-601, 2011.

[6] Y.Wang, H. Li, X. Luo, Q. Sun, and J. Liu "A 3D Fingerprinting Positioning Method Based on Cellular Networks," International Journal of Distributed Sensor Networks, p. 248981, 2014.

[7] M. Vieira, M. A. Vieira., P. Louro., P. Vieira, and A. Fantoni, "Fine-grained indoor localization: optical sensing and detection," Proc. SPIE 10680, Optical Sensing and Detection V, 106800H, 9 May 2018.

[8] A. Jovicic, J. Li, and T. Richardson, "Visible light communication: opportunities, challenges and the path to market," Communications Magazine, IEEE, vol. 51, no. 12, pp. 26–32, 2013.

[9] M. A. Vieira, M. Vieira, P. Louro,V. Silva, and P. Vieira, , "Optical signal processing for indoor positioning using a-SiCH technology," Opt. Eng. 55 (10), 107105, 2016.

[10] M. A. Vieira, P. Louro, M. Vieira, A. Fantoni, and A. Steiger-Garção, "Light-activated amplification in Si-C tandem devices: A capacitive active filter model," IEEE sensor journal, 12, NO. 6, pp. 1755-1762, 2012.

[11] S. B. Park, et al., "Information broadcasting system based on visible light signboard," presented at Wireless and Optical Communication 2007, Montreal, Canada, 2007.

[12] Y. Zhu, W. Liang, J. Zhang, and Y. Zhang, "Space-Collaborative Constellation Designs for MIMO Indoor Visible Light Communications," IEEE Photonics Technology Letters, vol. 27, no. 15, pp. 1667–1670, 2015.

[13] M. Vieira, M. A. Vieira., P. Louro., P. Vieira, A. Fantoni, "Light-emitting diodes aided indoor localization using visible light communication technology," Opt. Eng. 57(8), 087105, 2018.

[14] M. A. Vieira, M. Vieira, P. Louro, P. Vieira, "Bi-directional communication between infrastructures and vehicles through visible light," Proc. SPIE 11207, Fourth International Conference on Applications of Optics and Photonics, 112070C (3 October 2019); doi: 10.1117/12.2526500. 2019.

[15] M. Vieira, M. A. Vieira, P. Louro, A. Fantoni, P. Vieira, "Dynamic VLC navigation system in Crowded Buildings", International Journal On Advances in Software, v 14 n 3&4, pp. 141-150, 2021.

[16] M. Vieira, M. A. Vieira, P. Louro, A. Fantoni, P. Vieira, "Geolocation and communication in unfamiliar indoor environments through visible light", Proc. SPIE 11706, Light-Emitting Devices, Materials, and Applications XXV, 117060P (5 March 2021)

Parameter Optimization for BLE Mesh Sensor Networks Using an MQTT Gateway

Philipp Bolte
Dept. of Electronics and Circuit Technology
South Westphalia University of Applied Sciences
Soest, Germany
bolte.philipp@fh-swf.de

Ulf Witkowski
Dept. of Electronics and Circuit Technology
South Westphalia University of Applied Sciences
Soest, Germany
witkowski.ulf@fh-swf.de

***Abstract*— The BLE Mesh standard is well suited for use in IoT applications because of its low energy consumption. The Mesh extension enables communication beyond directly connected devices. The provisioning of the network can be performed using a smartphone utilizing a compatibility layer for traditional BLE. Connectivity to the Internet is required for many Internet of Things applications, which is not supported by BLE Mesh by default. We propose a bidirectional BLE Mesh to MQTT Gateway (GW) architecture to overcome this limitation. We have evaluated the effect of several BLE Mesh parameters on packet loss using the proposed GW architecture.**

Keywords—Mesh Networks, Internet of Things, Sensor Node, BLE Mesh, MQTT

I. INTRODUCTION

The smart home industry is growing at a rapid pace. In Europe, the number of smart homes increased from 83.9 million to 111.9 million from end of 2018 to end of 2019 while an annual increase of 20.2% is excepted until 2024 [1]. Similar growth is also predicted for the smart building sector. For Europe, the market share of smart building sector is estimated to grow at an annual rate of 17.6% from 2021 to 2028 [2]. Smart home and smart building are a segment of the Internet of Things (IoT) with special characteristics and requirements. Protocols traditionally used for smart building, e.g., BACnet, DALI or KNX, are using wired connections [3]. Those wired networks are inflexible and their expansion is often not easy to realize. Wireless protocols targeted for smart home applications, e.g., ZigBee, Z-Wave or Wi-Fi, are widely used [4]. Those systems can be retrofitted comparatively easily to existing buildings. However, these IoT protocols, except for Wi-Fi, require a sophisticated configuration. Furthermore, most of the wireless protocols are not designed for battery operated devices in terms of power consumption.

We propose a Bluetooth Low Energy (BLE) Mesh based sensor network for the use with smart building and smart home that solves the previous mentioned issues. This mesh extension of the BLE standard implements a flooding algorithm to forward messages across the network, so participants who are not in direct reach can communicate with each other. Low-power nodes with a very low current consumption enable the integration into battery powered devices. One key advantage of using BLE Mesh is the ability to configure the network using a smartphone or laptop without the need of additional accessory. The BLE Mesh standard further defines the application layer, providing interoperability between devices of different manufactures. We have designed a Gateway (GW) that forwards messages between the BLE Mesh network and a Message Queuing Telemetry Transport (MQTT) broker, e.g., for integration into cloud-based services or for bridging multiple spatial separated networks.

The second Section of the paper gives an introduction of the BLE Mesh standard with focus on IoT relevant features. The third Section introduces the proposed BLE Mesh to MQTT GW. In Section 4, the used set-up for the experiments is described. The results of the experiments are evaluated in Section 5. Section 6 concludes the paper.

II. BLE MESH

The BLE Mesh standard is based on the Bluetooth low-energy part of the Bluetooth 4.0 specification and shares the lower protocol layers [5]. Bluetooth devices usually implement a point-to-point connection between one central and multiple peripherals. In contrast, in a BLE Mesh network each device is able to communicate with all reachable devices of the network. The protocol stack of BLE Mesh is shown in Figure 1.

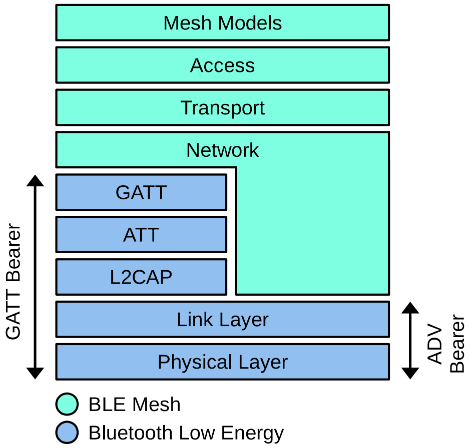

Figure 1. BLE Mesh protocol stack [5]

The lower two levels of BLE Mesh are shared with traditional BLE. The bearer level implements the transport of Protocol Data Units (PDU) using either advertisement packets of BLE at fixed time intervals or Generic Attribute (GATT) profiles for communication with legacy BLE devices. Packets are encrypted on network layer with a network key. The decrypted packets are retransmitted by the relay nodes while the Time-To-Live (TTL) field is decremented until it reaches zero.

This flooding approach does not require knowledge of the network structure. However, this approach is resulting in poor performance issues that can lead to an increased packet loss for large networks with many participants [7]. The simplicity, on the other hand, is especially beneficial for resource constraint devices typically used in IoT. The transport layer implements message segmentation, buffering of messages for coupled Low-Power Nodes (LPNs) that are currently not reachable, and encryption of the data from upper layers with application specific keys. The application specific encryption enables multiple isolated applications within a single network. Messages are retransmitted by the relay nodes even if the corresponding application key is not known. A BLE Mesh device can integrate multiple elements that are identified by a unique address. An element is an addressable unit, e.g., a switch panel with multiple buttons, in a BLE Mesh network. Each element includes one or multiple models. The models exchange data by a publish and subscribe pattern. BLE defines various mesh models with standardized attributes. Data producing devices usually implement some sort of server model. Data consuming devices, on the other hand, typically implement a client model. There are many predefined models, ranging from generic on/off or level models to very specific models, e.g., for lighting applications [8]. For the proposed application, we are using a sensor server for the temperature sensor nodes and sensor clients for the display nodes. The GW implements both, a sensor client to fetch sensor data and a sensor server to transmit requests from MQTT to a BLE Mesh device.

A. *Message Transport*

The maximum size of access PDUs is 380 bytes, while packets above 11 bytes are segmented by the network layer [9]. The performance of segmented messages is poor compared to unsegmented messages [10]. The transport PDUs of segmented messages are not transmitted instantly but rather in successive BLE advertise packets. Therefore, it is reasonable to send the data in several smaller access layer messages, as the overhead is negligible. In this case, a lost transport PDU affects only a single measurement and not a complete data series.

Figure 2 shows the transfer of BLE Mesh transport PDUs using the Advertising (ADV) bearer. The advertiser, i.e., sender, transmits the transport PDU in three identical *ADV_NONCONN_IND* packets on BLE channels 37, 38 and 39, that are primary used for BLE advertisement. The sequence of packets is determined by the fixed *advInterval*, that is between 20 ms and 10.24 s, and a random delay *advDelay* between 0 and 10 ms [11]. The scanner, i.e., receiver, listens successively on the advertisement channels for the time *scanWindow* with an interval defined by *scanInterval*.

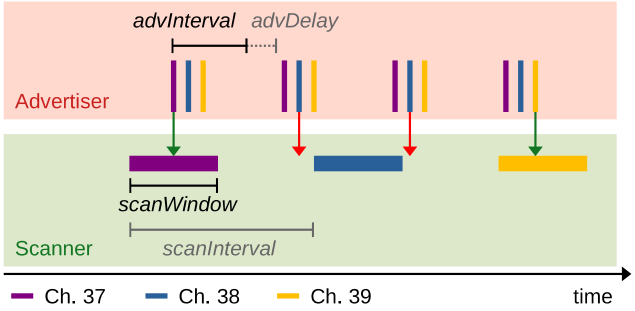

Figure 2. BLE Mesh data transfer using ADV bearer

Since the receiver does not listen permanently, the data must be sent multiple times to ensure reception. BLE Mesh implements three types of retransmissions [12]. The retransmission of network PDUs sent by the note is controlled by the *Network Transmission Count* (NTC), which allows 1 to 8 transmissions, and *Network Transmit Interval* (NTI), in a range between 10 to 320 ms. The retransmission of received network PDUs from other nodes of the network is controlled by the parameters *Relay Retransmit Count* (RRC) and *Relay Retransmit Interval* (RRI), having the same range as for network scope. On model layer, the retransmission of published messages is controlled by the *Publish Retransmit Count* (PRC) and *Publish Retransmit Interval* (PRI), ranging from 50 ms to 1.6 s. A message can be sent up to 64 times if the network and publish retransmit count parameters are set to maximum.

B. *Device Addressing*

Messages, respectively transport PDUs, have a source and a destination address, which are both 16 bit wide. Each node of a network is assigned a unique unicast address during provisioning in the address range from 0x0001 to 0x7FFF, which is half of the available address space. Furthermore, various multicast address spaces are available. The address space between 0x8000 and 0xBFFF is reserved for virtual addresses. Those addresses represent a 128 bit Universally Unique Identifier (UUID) that can be used by manufactures to uniquely address elements of their products. However, this function has been barely used so far. Addresses starting from 0xC000 are used as group addresses. This address range is further subdivided to assignable addresses up to 0xFEFF and special addresses, e.g., 0xFFFE for all relays and 0xFFFF for all nodes [14]. E.g., the assignable group address could be used for assigning all devices of a certain room.

Incoming messages with the unicast address of the receiving node are always processed by the device. The models of a node can additionally subscribe to virtual addresses and group addresses. For outgoing messages, either a unicast or a multicast address can be used as destination.

C. *Low-Power Features*

The BLE standard by itself is already optimized for low energy consumption. The BLE Mesh specification introduces additional low-power features. E.g., a node can operate as LPN to further increase battery runtime. This type of node couples with a friend node and suspends the scanning for advertisement packets. The LPN periodically polls the permanent listening friend node for messages that were received since the last polling. The polling interval can be set between 10 s and several hours. The LPN enters the lowest possible power state between polling and is not reachable by other nodes.

D. *Network Provisioning*

A provisioner node is used to set-up the network. The provisioning process involves five stages. First, the unprovisioned devices announce their presence by sending mesh beacons. The provisioner sends an invitation which is replied by a capabilities report from the device. In the key exchange stage, both devices exchange their public keys. It is recommended to perform an authentication, e.g., by a pin code afterwards. This step can be skipped if the devices are not able to interact with the user. The actual provisioning is performed by the provisioner by setting the network and application keys and a unicast address and optionally configure the models. Afterwards the device has joined the network and is able to send and receive messages.

E. *BLE Connectivity*

By default, the BLE Mesh nodes are communicating by embedding the network PDUs inside of *ADV_NONCONN_IND* advertisement packets. The hardware of legacy BLE devices, e.g., Smartphones is, in theory, capable of processing those packets but the software stack does not support the BLE Mesh protocol. To enable communication with those legacy devices, the BLE Mesh standards provides a GATT proxy feature. The network PDUs are then transmitted using the Mesh Proxy GATT service (0x1828) [15]. Typically, the provisioning of new nodes is performed using a smartphone utilizing the GATT proxy feature for easy management of the network. The GATT proxy feature is optionally and does not need to be implemented by the nodes.

III. MQTT GATEWAY

BLE Mesh devices are only capable of sending messages to other nodes of a network. For typical IoT applications, an integration of cloud services is at least desired, if not mandatory. The integration of cloud services, e.g., could enable a deeper analysis of sensor data for process optimization and remote control of actuators [16]. Our proposed GW enables the integration of low-power BLE Mesh nodes into online cloud services using the widely used MQTT protocol.

Figure 3 shows the components of our BLE Mesh to MQTT GW solution. The hardware of the system is composed of a Raspberry Pi miniature computer and a Nordic nRF52840 BLE development board. The Raspberry Pi itself embeds a Bluetooth radio which cannot be used as the software stack since is not Mesh compatible.

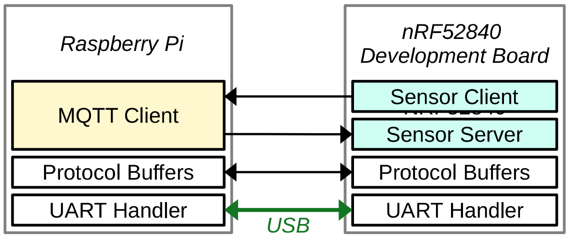

Figure 3. BLE Mesh to MQTT GW components

A. *BLE Mesh Endpoint*

The nRF52840 BLE development kit (DK) acts as the BLE Mesh Endpoint (EP) of our proposed GW. The nRF52840 System-on-Chip (SoC) of the DK embeds a 2.4 GHz radio and an ARM Cortex-M processing core. The developed BLE Mesh EP was derived from application examples of the Zephyr framework. We have implemented a generic sensor client model. The non-uniform data representation for different sensor types does not allow a generic conversion between BLE sensor values and standard floating point format [17]. We have implemented hooks for sensor types *present ambient humidity*, *precise present ambient temperature* and *present input voltage*. The integration of other sensor types can be achieved by implementing according hooks with data conversion to a generic float value. The sensor client is able to receive messages from multiple devices by subscribing to a group address (e.g., 0xC000). All received sensor readings are redirected to the MQTT EP after adding meta information, e.g., the sender address and Received Signal Strength Indicator (RSSI). Incoming messages from the MQTT EP are redirected to other BLE Mesh nodes by the implemented sensor server. Currently, only the above listed sensor types are supported for sending messages from MQTT to a BLE Mesh node. The integration of other sensor types requires the extension of the sensor server model. A final version of the GW would implement all defined sensor types. The destination address of the redirected sensor values is fetched from the included meta data included in the MQTT message. The configuration of the model parameters is performed by the provisioner of the network.

B. *MQTT Endpoint*

The MQTT protocol is based on TCP/IP stack. The used nRF52840 SoC does not support Ethernet or Wi-Fi interface. Therefore, the MQTT EP is executed on a Raspberry Pi miniature computer that integrates an Ethernet interface. Newer models also integrate a Wi-Fi module. The software of the MQTT EP is written in Python and utilizes the threading library to prevent I/O blocking. The Python program reads the required connections parameters from a configuration file. The configuration file includes the MQTT broker address, user credentials and a topic prefix to enable the use of multiple GWs on a single MQTT broker. Incoming JSON formatted messages from the MQTT broker are parsed to a Protobuf object that is then transferred to the BLE EP using the serial handler. The MQTT protocol was designed for ASCII-formatted payload, while Protoc serializes to a binary representation. Furthermore, Protoc is not supported by all cloud stacks. Therefore, the MQTT payload is JSON formatted, to enhance compatibility. Since the message objects are no longer specified by a hard-coded protocol definition, it is now the responsibility of the developer to correctly format the JSON message. Incorrectly formatted messages are discarded by the broker. All received sensor values from the BLE Mesh EP are parsed to a JSON object that is published by the MQTT client. The topic of the message includes the source address of the BLE Mesh message. Additional meta data, e.g., RSSI, is included in the payload, as shown in Figure 4.

```
{
     "seq": 236,
     "timestamp": 29470814,
     "addr": 31,
     "recvRssi": -86,
     "recvTtl": 6,
     "ambientHumidity": {
       "ambientHumidity": 33.91
     }
}
```

Figure 4. MQTT message payload example

C. *Internal Message Coding*

The messages transfer between the BLE Mesh EP and the MQTT EP is realized using Google Protocol Buffers (Protobuf) format. With Protobuf, structured data objects, that are specified in a platform independent ".proto"-file, can be translated to different programming languages using the Protocol Buffers compiler (protoc) [18]. The same protocol definition can be used in both, the C program on the BLE SoC and the Python program on the Raspberry Pi. In the C program, the data objects are represented by structures. In Python each defined data object is represented by a class that can be instantiated. The Protobuf library serializes those structured data objects to a binary stream that can be deserialized by the receiver. The Protoc data format is substantially more efficient compared to the common used JSON protocol and usually only produces negligible overhead [19]. The capacity of the UART connection between the Raspberry Pi and the nRF52840 board is limited to 115200 bauds, therefore an efficient data transfer minimizes packet delay and ensures good utilization of the limited UART link.

IV. REFERENCE SET-UP

A reference BLE Mesh network was set-up to evaluate the use of BLE Mesh for indoor IoT applications. We have deployed a typical smart home environment with multiple low-power and relay nodes, as shown in Figure 5. The proposed GW architecture was used to track messages inside the mesh network and to collect meta data.

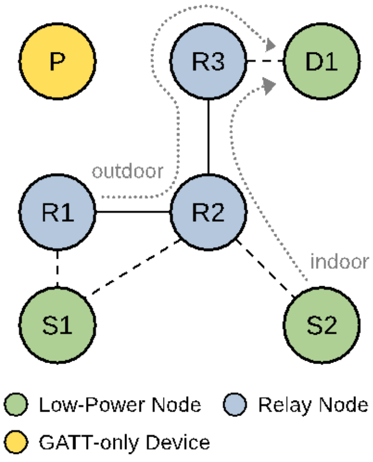

Figure 5. BLE Mesh reference set-up

The mesh network is made up of two LPN acting as temperature and humidity sensors. One LPN is equipped with an e-paper display that shows sensor readings that were transferred over the BLE Mesh network. The LPNs have no direct connection, instead three relay nodes are used to bridge all devices. Each relay acts as an MQTT GW. The LPNs establish a friendship with one of the relay nodes in reach to further reduce energy consumption. The display LPN implements a sensor client that subscribes to a group address (0xC000). The display is divided into two slots. One dataset is gathered from the mesh-local sensor *S1* (indoor) and the dataset for the second slot is injected from MQTT by router *R1* (outdoor). In this example, the second dataset is fetched from OpenWeather Application Programming Interface (API). The LPN sensors gather temperature and humidity readings each 15 minutes. The outdoor temperature and humidity is fetched at an interval of 30 minutes from the web API. The transmission of BLE Mesh messages inside the network can be tracked as each relay redirects incoming messages to the MQTT broker.

V. EXPERIMENTS

We have evaluated the reliability of the data transmission based on the previously described set-up. The packet loss was used as the primary metric. The received meta data from the GWs was evaluated as well. The received RSSI values provide additional information about the link reserve. The experiments were primarily conducted to study the effect of retransmission settings. A high number of repetitions increases the probability that a message will reach the recipient. On the other hand, the medium is shared by all participants of the network. The total transmitted messages increase exponentially with the number of participants and the transmit count values, increasing the probability for collisions.

In total, three experiments were performed in an office building under real conditions. The experiments were carried out consecutively for a period of 7 days using the same hardware. Table 1 shows the used parameters for the experiments.

TABLE I. BLE MESH PARAMETERS

	Exp. 1	**Exp. 2**	**Exp. 3**
PTC	1	1	-
PTI [ms]	250	500	-
NTC	3	6	2
NTI [ms]	50	50	50
RRC *	3	6	2
RRI * [ms]	60	60	60

* only for relay nodes

Figure 6 shows the packet loss of the three experiments for the transmissions of LPN S1. The LPN S1 transmits three messages each 15 minutes, reporting its battery voltage, ambient temperature and humidity. The messages are first received by relay node R1 and get retransmitted until they finally reach the display node D1. The messages are tracked by the GWs.

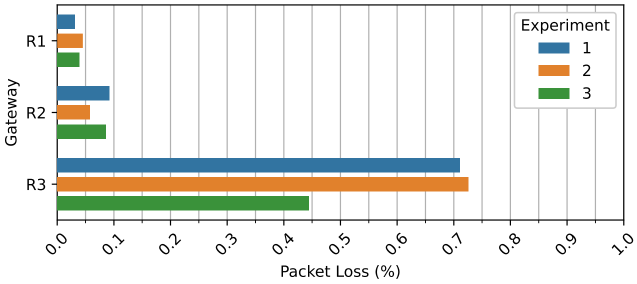

Figure 6. Packet loss for messages from LPN S1

The packet loss at the first relay node is less than 5% for all parameter sets. The loss increases to almost 10% for all experiments at node R2. Up to this point, however, no major differences are discernible between the various parameter sets. Significant differences could be observed between the transmissions from relay nodes R2 to R3. Here, the packet loss of experiments 1 and 2 is around 70%. In the last experiment, the packet loss at R3 was 44.5% although the transmit counter was set lowest. Figure 7 shows boxplots of the RSSI parameter of the received messages sent by LPN S1.

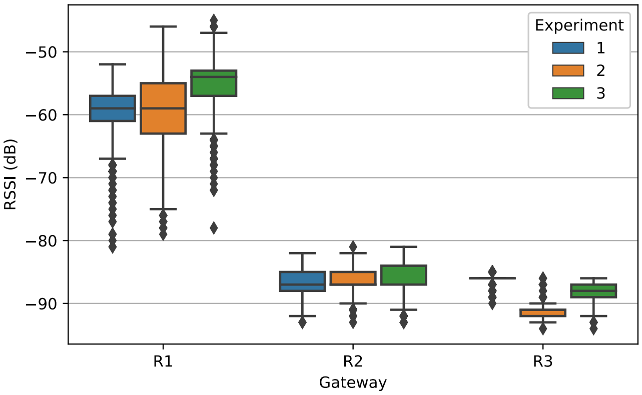

Figure 7. RSSI distribution for messages from LPN S1

The RSSI values of the received messages from S1 at relay node R1 are widely spread. The mean value ranged from -55.2 dB for Experiment 3 to -59.4 dB for Experiment 1. At stations R2 and R3 a smaller spread of the recoded RSSI values was observed. The mean values were located around -86 dB for station R2 for all experiments. For node R3 the mean values of the RSSI measurements are between -86 dB for experiment 1 and -91 dB for experiment 2. The smallest recorded RSSI value was –94 dB. The sensitivity of the used nRF52840 module is specified with -95 dB [20]. The spatial conditions used for the experiments demonstrate a reliable transmission with a link margin of 10 dB. Compared to the significantly better signal strengths at station R1, no increased packet loss could be detected. For stations that are just in reach, however, the presence of a small interferer is sufficient to interrupt the transmissions. The scatter of successive RSSI values was rather small. However, there were occasional jumps in the measured values, which can be explained by the presence of interferer. Then the signal of all messages is suppressed to the extent that they can no longer be decoded by the receiver. In such cases, the increase of transmission counters does not improve reachability. If sufficient link margin is available, the already low packet loss will not be significantly improved by the increase of transmissions.

VI. CONCLUSIONS AND FUTURE WORK

The proposed GW architecture provides connectivity between a BLE Mesh network and the Internet. The provisioning of the network can be done via smartphone. Only the MQTT parameters need to be set in a configuration file on the GW. Even existing networks can be easily connected to the Internet using the proposed GW architecture. The GW includes meta data of the received BLE Mesh messages before redirection to the MQTT broker. The proposed GW architecture can be used to perform experiments on BLE Mesh networks without the need for expensive measurement equipment.

We have evaluated the effect of transmission counters and delays on packet loss when transmitting data over multiple hops. A BLE Mesh node does not listen continuously on the RF interface but instead implements a complex scheduling of scan intervals on multiple channels to reduce current consumption. A re-transmission of messages, in theory, should improve reliability. However, too many repetitions lead to a high utilization of the radio channel. Our experiments have shown that the receiver of the used nRF52840 module works very reliably with little packet loss, even at the lowest possible packet repetition rates, if sufficient link margin is given. In such cases, an increase repetition of messages does not improve the packet loss. The experiments were performed under real conditions. We could observe a significant drop of RSSI values for longer time periods on all relay nodes, caused by the presence of disturbers, e.g., Wi-Fi and other BT devices located in the lab. When a station is positioned close to the range limit, the decreased signal strength cannot be compensated by increasing the repetition counters, resulting in high packet loss during the presence of the disturber. Our recommendation is to set the corresponding parameters as small as possible, in order to reduce the RF channel utilization as low as possible.

The proposed architecture could be extended to detect packet loss between multiple GWs and to retransmit lost messages using the MQTT link. However, the flooding of the mesh network with always the same message must be prevented.

REFERENCES

[1] M. Bäckman, “Smart Homes and Home Automation - IoT Research Series,” Berg Insight, Gothenburg, Sweden, 2021.

[2] “Europe Smart Building Market Size, Share & COVID-19 Impact Analysis, By Solution, By Application, and Europe Forecast, 2021-2028,” Furtune Business Insights, Apr. 2021.

[3] K. Lohin, Y. Jain, C. Patel, and N. Doshi, “Open Communication Protocols for Building Automation Systems,” in *Procedia Computer Science*, vol. 160, Nov. 2019, pp. 723-727, doi: 10.1016/j.procs.2019.11.020.

[4] S. J. Danbatta, A. Varol, “Comparison of Zigbee, Z-Wave, Wi-Fi, and Bluetooth Wireless Technologies Used in Home Automation,” in *2019 7th International Symposium on Digital Forensics and Securits (ISDF)*, Jul. 2019, pp. 1-5, doi: 10.1109/ISDFS.2019.8757472.

[5] Nordic, *nRF SDK for Mesh v3.2.0*, Accessed: Nov. 19, 2021. Accessed: Mar. 02, 2022. [Online]. Available: https://infocenter.nordicsemi.com/topic/com.nordic.infocenter.meshsdk.v3.2.0/md_doc_introduction_basic_concepts.html

[6] S. M. Darroudi, C. Gomez, and J. Crowcroft, “Bluetooth Low Energy Mesh Networks: A Standards Perspective,” in *IEEE Communications Magazine*, vol. 58, Apr. 2020, pp. 95-101, doi: 10.1109/MCOM.001.1900523.

[7] R. Rondón, A. Mahmood, S. Grimaldi, and M. Gidlund, “Understanding the Performance of Bluetooth Mesh: Reliability, Delay, and Scalability Analysis,” in *IEEE Internet of Things Journal*, vol. 7, Mar. 2020, pp. 2089-2101, doi: 10.1109/JIOT.2019.2960248.

[8] *Bluetooth Specification - Mesh Model*, rev. 1.0.1, Jan. 2021. Accessed: Mar. 02, 2022. [Online]. Available: https://www.bluetooth.com/specifications/specs/mesh-model-1-0-1.

[9] Á. Hernández-Solana, D. Pérez-Díaz-De-Cerio, M. García-Lozano, A. V. Bardají, and J. Valenzuela, "Bluetooth Mesh Analysis, Issues, and Challenges," in *IEEE Access, vol. 8*, pp. 53784-53800, 2020, doi: 10.1109/ACCESS.2020.2980795.

[10] A. Aijaz, A. Stanoev, D. London, and V. Marot, “Demystifying the Performance of Bluetooth Mesh: Experimental Evaluation and Optimization”, in in *IEEE Wireless Days 2021*, Preprint

[11] Rohde & Schwarz, “Bluetooth Low Energy Over-The-Air Advertiser Testing,” Application Note, Rev. 1C109, Dec. 2017.

[12] *Bluetooth Specification - Mesh Profile*, rev. 1.0.1, Jan. 2019. Accessed: Mar. 02, 2022. [Online]. Available: https://www.bluetooth.com/specifications/specs/mesh-profile- 1-0-1.

[13] M. Woolley, „Bluetooth Mesh Networking: An Indtoduction for Developers," Version 1.0.1, Dec 2020. Accessed: Mar. 02, 2022. [Online]. Available: https://www.bluetooth.com/wp-content/uploads/2019/03/Mesh-Technology-Overview.pdf.

[14] Kai R. and M. Woolley, „The Fundamental Concepts of Bluetooth Mesh Networking", Aug. 2017. Accessed: Mar. 02, 2022. [Online]. Available: https://www.bluetooth.com/blog/the-fundamental-concepts-of-bluetooth-mesh-networking-part-2/.

[15] *Bluetooth Specification – 16-bit UUID Numbers Document*, Jan. 2022. Accessed: Mar. 02, 2022. [Online]. Available: https://btprodspecificationrefs.blob.core.windows.net/assigned-values/16-bit%20UUID%20Numbers%20Document.pdf

[16] A. Rajith, S. Soki, and M. Hiroshi, „Real-time optimized HVAC control system on top of an IoT framework," in *2018 Third International Conference on Fog and Mobile Edge Computing (FMEC)*, Barcelona, Spain, Apr. 2018, pp. 181-186, DOI: 10.1109/FMEC.2018.8364062 .

[17] Nordic, *nRF Connect SDK*, Accessd: Mar. 16, 2022. [Online]. Available: https://developer.nordicsemi.com/nRF_Connect_SDK/doc/latest/nrf/libraries/bluetooth_services/mesh/sensor_types.html

[18] Google, *Protocol Buffers Language Guide*, Mar. 06, 2022. [Online]. Available: https://developers.google.com/protocol-buffers/docs/proto3

[19] S. Popić, D. Pezer, B. Mrazovac, and M. Teslic, „Performance evaluation of using Protocol Buffers in the Internet of Things communication," in *2016 International Conference on Smart Systems and Technologies (SST)*, Oct. 2016, pp. 261-265.

[20] Nordic, „High-end multiprotocol Bluetooth Low Energy (LE) SoC supporting: Bluetooth 5.3 / Bluetooth mesh / Thread / Zigbee / 802.15.4 / ANT," nRF52840 Product Brief, Rev. 3.0. Accessed: Mar. 02, 2022. [Online]. Available: https://nsscprodmedia.blob.core.windows.net/prod/software-and-other-downloads/product-briefs/nrf52840-soc-v3.0.pdf

Visible Light Communication in Vehicular Communication Applications

Manuel Augusto Vieira, Manuela Vieira, Paula Louro,
ADETC/ISEL/IPL,
R. Conselheiro Emídio Navarro, 1959-007
Lisboa, Portugal
CTS-UNINOVA
Quinta da Torre, Monte da Caparica, 2829-516,
Caparica, Portugal

e-mail: mv@isel.pt, mv@isel- ipl.pt, plouro@deetc.isel.pt,

Pedro Vieira
ADETC/ISEL/IPL,
R. Conselheiro Emídio Navarro, 1959-007
Lisboa, Portugal
Instituto das Telecomunicações
Instituto Superior Técnico, 1049-001,
Lisboa, Portugal
e-mail: pvieira@isel.pt

Abstract— This paper addresses the issues related to the Visible Light Communication (VLC) usage in vehicular communication applications. We propose a Visible Light Communication system based on Vehicle-to-Vehicle, Vehicle-to-Infrastructure and Infrastructure-to-Vehicle communications able to safely manage vehicles crossing through an intersection. By using the streetlamps, street lights and traffic signaling to broadcast information, the connected vehicles interact with one another and with the infrastructure. Using joint transmission, mobile optical receivers collect data, calculate their location for positioning and, concomitantly, read the transmitted data from each transmitter. As receivers and decoders, optical sensors with light filtering properties, are used. Bidirectional communication between the infrastructure and the vehicles is tested. To command the passage of vehicles safely queue/request/response mechanisms and temporal/space relative pose concepts are used. The results show that the innovative solutions for congested intersections are related to the introduction of split intersections. The results indicate that the V-VLC system increases safety by directly monitoring critical points such as queue formation and dissipation, relative speed thresholds, as well as inter-vehicle spacing.

.

Keywords- Vehicular Communication; Split Intersection; Queue distance; Vehicle Pose Connectivity; Vehicular-Visible Light Communication (V-VLC); White LEDs, SiC photodetectors; Traffic control.

I. INTRODUCTION

Vehicles can connect to others, or to the infrastructure, providing an Internet connection [1]. In this area, VLC have a great potential for applications due to their relatively simple design for basic functioning, efficiency, and large geographical distribution.

The main objective of the Intelligent Transport System (ITS) technology is to optimize traffic safety and efficiency on public roads by increasing situation awareness and mitigating traffic accidents through vehicle-to-vehicle (V2V) and vehicle-to-infrastructure (V2I) communications [2] [3] [4]. By knowing, in real time, the location, speed and direction of nearby vehicles, a considerable improvement in traffic management is expected. The goal is to increase the safety and throughput of traffic intersections using cooperative driving. Intersections, by their nature, easily become traffic bottlenecks and conflict areas because they usually cause considerable delays due to congestion problems. In the split intersection, the conventional four-legged intersection is replaced by two separate lighter intersections which facilitate a smoother flow with less driver delay [5][6].

VLC is an emerging technology [7][8] that enables data communication by modulating information on the intensity of the light emitted by LEDs. In the case of vehicular communications, the use of VLC is made easier because all vehicles, street lights, and traffic lights are equipped with LEDs, using them for illumination. Here, the communication and localization is performed using the street lamps, the traffic signaling and the head and tail lamps, enabling the dual use of exterior automotive and infrastructure lighting for both illumination and communication purposes [9][10].

Our work focuses directly on the use of VLC as a support for the transmission of information providing guidance services and specific information to drivers. A Vehicle-to-Everything (V2X) traffic scenario is simulated and bidirectional communication between the infrastructure and the vehicles is tested, using the VLC request/response concept. Every vehicle is equipped with a receiver module for receiving the mapped information generated from the street lamps. The receiver modules include a photodetector based on a tandem a-SiC:H/a-Si:H pin/pin light controlled filter [11][12] that multiplex the different optical channels, perform different filtering processes (amplification, switching, and wavelength conversion) and decode the encoded signals, recovering the transmitted information. Here, the streetlights and traffic lights, through VLC, report its geographical positions and specific information to the drivers since its infrastructure can also be reused to embed the edge/fog nodes in them. Cooperative localization is realized in a distributed way with the incorporation of the indirect V2V relative pose estimation method. The vehicle gathers relevant data from neighboring vehicles and estimates the relative pose of them using the indirect V2V relative pose.

This paper is organized as follows. After the introduction, in Section 2, the V-VLC system is described and the scenario, architecture, communication protocol, coding/decoding techniques analyzed. In Section 3, the experimental results are reported and the system evaluation performed. A phasing traffic flow diagram based on V-VLC is developed, as a Proof of Concept (PoC), to control the arrival of vehicles to the split intersection. Finally, in Section 4, the main conclusions are presented.

II. V-VLC VEHICULAR COMMUNICATION

While V2V links are particularly important for safety functionalities such as pre-crash sensing and forward collision warning, I2V links provide the connected vehicles with a variety of useful information [13] [14].

A. *System Design*

The system is composed by two modules: the transmitter and the receiver located at the infrastructures and at the driving cars. The block diagram and the transmitter and receiver relative positions of the V-VLC system are presented in Figure 1.

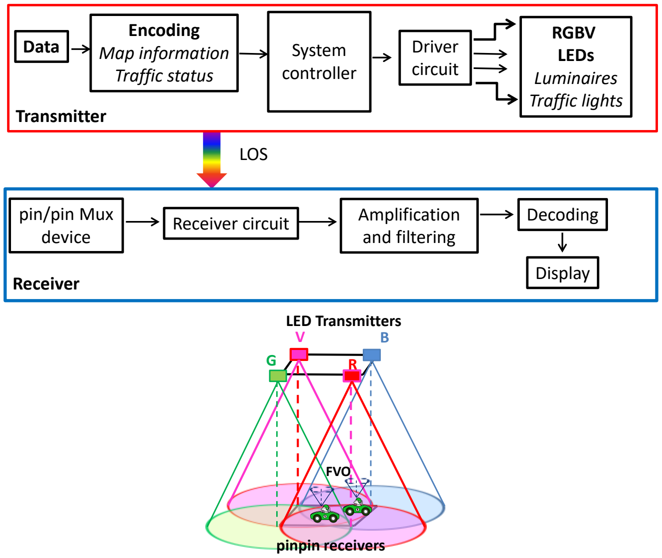

Figure 1. Block diagram and transmitters and receivers 3D relative positions.

Both communication modules are software defined, where modulation/ demodulation can be programed. In the transmission side, a modulation and conversion from digital to analog data is done. An On-Off Keying (OOK) modulation scheme was used to code the information [15] [16].The visible light emitted by the LEDs passes through the transmission medium and is received by the MUX device. White light tetra-chromatic sources are used providing a different data channel for each chip. Each luminaire is composed of four white LEDs framed at the corners of a square (see Figure 1). At each node, only one chip of the LED is modulated for data transmission, the Red (R: 626 nm), the Green (G: 530 nm), the Blue (B: 470 nm) or the Violet (V). Modulation and digital-to-analog conversion of the information bits is done using signal processing techniques.

The coverage map for a square unit cell is displayed in Figure 2. The LEDs are modeled as Lambertian sources where the luminance is distributed uniformly in all directions, whereas the luminous intensity is different in all directions [17].

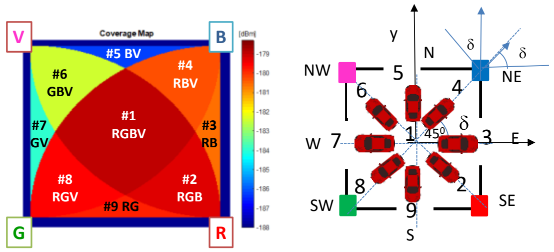

Figure 2. Illustration of the coverage map in the unit cell: footprint regions (#1-#9) and steering angle codes (2-9).

The input of the aided guidance system is the coded signal sent by the transmitters to an identify vehicle, and includes its position in the network $P(x, y)$, inside the unit cell and the steering angle, δ, that guides the driver across his path. The device receives multiple signals, finds the centroid of the received coordinates, and stores it as the reference point position. Nine reference points, for each unit cell, are identified giving a fine-grained resolution in the localization of the mobile device across each cell (see Figure 2). The VLC photosensitive receiver is a double pin/pin photodetector based on a tandem heterostructure, p-i'-n/p-i-n sandwiched between two conductive transparent contacts. Exposed to light, the device offers high sensitivity and linear response, generating a proportional electrical current.

B. *Architecture, Scenario and Multi-Vehicle Cooperative Localization*

In Figure 3a, the proposed architecture is illustrated. Under this architecture, the short-range mesh network purpose is twofold: enable edge computing and device-to-cloud communication, by ensuring a secure communication from a luminaire controller to the edge computer or datacenter (I2IM), through a neighbor traffic light controller with an active cellular connection; and enable peer-to-peer communication (I2I), to exchange information. It performs much of the processing on embedded computing platforms, directly interfacing to sensors and controllers. It supports geo-distribution, local decision making, and real-time load-balancing.

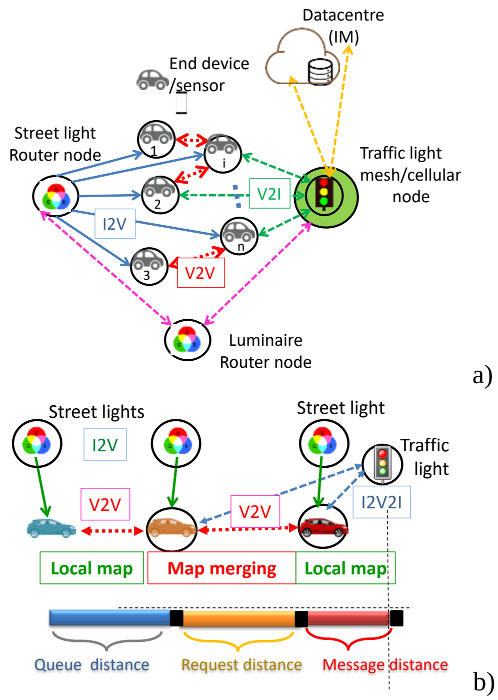

Figure 3. a) Mesh and cellular hybrid architecture. b) Graphical representation of the simultaneous localization and mapping problem using connectivity as a function of node density, mobility and transmission range.

A highly congested traffic scenario will be strongly connected. In order to determine the delay, the number of vehicles queuing in each cell at the beginning and end of the green time is determined by V2V2I observation, as illustrated in Figure 3b. Based on a truncated exponential distribution the distance, *d* between vehicles is calculated [18].

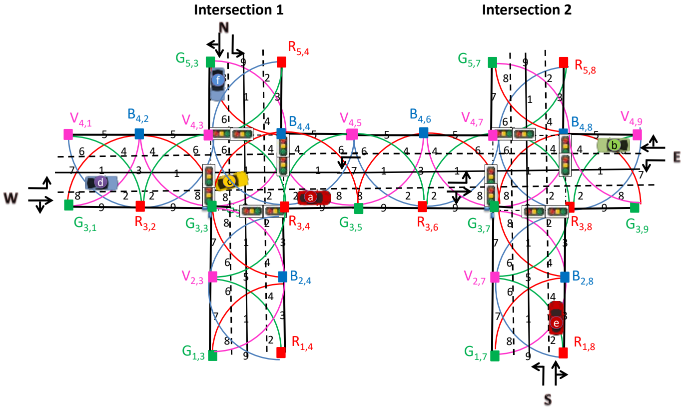

Figure 4. Simulated scenario. V2X optical infrastructure and generated joint footprints in a split crossroad (LED array=RGBV color spots).

The simulated scenario is a traffic light controlled split intersection as displayed in Figure 4. The grid size was chosen in order to avoid an overlap in the receiver from the data in adjacent grid points. Each transmitter, $X_{i,j}$, carries its own color, X, (RGBV) as well as its horizontal and vertical ID position in the surrounding network (i,j). In the PoC, was assumed that the split crossroad is located in the intersections of line 4 with column 3 and 7 (see Figure 4). The emitters are located at the nodes along the roadside. Thus, each LED sends a I2V message that includes the synchronism, its physical ID and the traffic information. When a probe vehicle enters the streetlight´s capture range, the receiver replies to the light signal, and assigns a unique ID and the traffic message [16].

Figure 4 illustrates the split intersection, which has only one main street connecting two crossroads (Intersection 1-Intersection 2). Four traffic flows were considered. One is coming from West (W) with three vehicles (*a*, *c*, *d*) approaching the crossroad, Vehicle *a* with straight movement and Vehicle *c* and Vehicle *d* with left turn only. In the second flow, Vehicle *b* from East (E), approaches the intersection with left turn only. In the third flow, Vehicle *e*, oncoming from South (S), has e right-turn approach. Finally, in the fourth flow, Vehicle *f*, coming from North, goes straight.

For the intersection manager crossing coordination, the vehicle and the IM exchange information through two types of messages, “request” (V2I) and “response” (I2V). Each driver, approaching the intersection area from each queue side has previously selected and stays in the appropriate lane for their destination (left turn only or shared by right-turn and through movements). Inside the request distance, an approach “request” is sent, using as emitter the headlights.

The request message is received and decoded by the receiver in the traffic light facing the lane (local controller) which is interconnected to the intersection manager (V2I). The “request” contains all the information that is necessary for a vehicle’s space-time reservation for its intersection crossing (speeds, and flow directions). Intersection manager uses this information to convert it in a sequence of timed rectangular spaces that each assigned vehicle needs to occupy the intersection. An intersection manager’s acknowledge is sent from the traffic signal over the facing receiver to the in car application of the head vehicle. Once the response is received (message distance in Figure 3b), the vehicle is required to follow the provided occupancy trajectories (footprint regions, see Figure 2). If a request has any potential risk of collision with all other vehicles that have already been approved to cross the intersection, the control manager only sends back to the vehicle (V2I) the “response” after the risk of conflict is exceeded.

There are critical points where traffic conditions change: the point at which a vehicle begins to decelerate when the traffic light turns red (message distance), the point at which it stops and joins the queue (queue distance), the point at which it starts to accelerate when the traffic light turns green (request distance) or the points at which the coming vehicle is slowed by the leaving vehicle. As a result, the road resistances can be calculated dynamically based on the relative pose positions of the vehicles and the traffic signal phase at intersections. With V2I2V communication, the travel time that influences traffic channelization in different routes can be calculated and real-time data about speed, spacing, queues, and saturation can be collected across the queue, request and message distances.Three types of information $q_i\ (t)$, $q_i\ (t,t')$ and $q_{ij}\ (t)$ compose the basic elements of a pose graph for multi-vehicle cooperative localization, t and t' are the request and cross times From a digital map we automatically extract a set of attributes that characterize an intersection: the poses, $q_i\ (x,\ y,\ t)$, the courses and traffic rules (stop, give way) [19, 20]. An Indirect V2V Relative Pose Estimation method is proposed in Figure 3b. Here, when two vehicles are in neighborhood, the geometric relationship between them can be indirectly inferred via a chain of geometric relationships among both vehicles' positions and local maps. The follower vehicle can be localized by itself, as in single vehicle localization, $q_i\,(t)$, and can also be localized by combining the localization result of vehicle leader and the relative localization estimate between the two vehicles, $q_{ij}\,(t)$. For a vehicle with several neighboring vehicles, it uses the indirect V2V relative pose estimation method to estimate the relative pose of each neighboring vehicle one by one.

In Figure 5, a color phasing diagram in split intersection is shown. We have assumed four "color poses" linked with the radial range of the modulated light in the RGBV crossroad nodes [20].

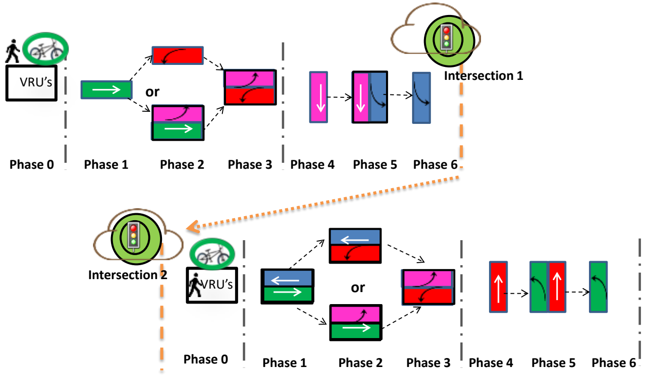

Figure 5 Phasing diagram in a split intersection

On the basis of the proposed phasing diagram, a phase for vulnerable road users (VRU's) only, as well as the separation of traffic flow in the North / South direction, allows the introduction of bike lanes at Intersection 1 (South and East straight movements) and Intersection 2 (North straight movements), reducing conflicts between vehicles and cyclists. The West straight, South left turn and West right turn maneuvers correspond to the "Green poses". "Red poses" are related with South straight, East left turn and South right turn maneuvers, "Blue poses" with East straight, North left turn and East right turn and finally "violet poses" with North straight, West left turn and North right turn maneuvers.

C. Communication Protocol and Coding/Decoding Techniques

To code the information, an On-Off keying (OOK) modulation scheme was used and it was considered a synchronous transmission based on a 64- bits data frame. The frame is divided into four, if the transmitter is a streetlamp or headlamp, or five blocks, if the transmitter is the traffic light. The first block is the synchronization block [10101], the last is the payload data (traffic message) and a stop bit ends the frame. The second block, the ID block gives the location (x, y coordinates) of the emitters inside the array ($X_{i,j,}$). Cell's IDs are encoded using a 4 bits binary representation for the decimal number. The δ block (steering angle (δ)) completes the pose in a frame time $q(x,y,\ \delta,\ t)$. Eight steering angles along the cardinal points and coded with the same number of the footprints in the unit cell (Figure 2) are possible from a start point to the next goal. If the message is diffused by the IM transmitter, a pattern [0000] follows this identification, if it is a request (R) a pattern [00] is used. The traffic message completes the frame.

Because the VLC has four independent emitters, the optical signal generated in the receiver can have one, two, three, or even four optical excitations, resulting in 2^4 different optical combinations and 16 different photocurrent levels at the photodetector. As an example, in Figure 6, the V2I MUX signals received and decode (on the top of the figures) is displayed for the split intersection. In the right side, the received channels are identified by its 4-digit binary codes and associated positions in the unit cell. On the top the transmitted channels packets [R, G, B, V] are decoded. In accordance with Figures 2 and 3, results show a request from vehicle a, when crossing Intersection 2 (Green pose; #2E: $R_{3,6}\,G_{3,7}$, $B_{4,6}\ \delta\ (3)$) under Phase 1.

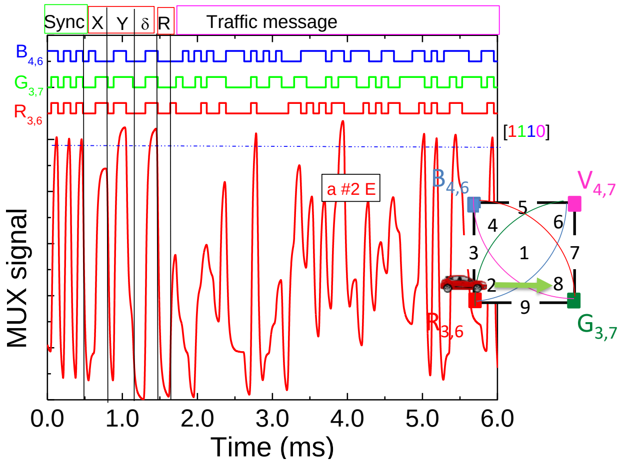

Figure 6 MUX signal and frame structure representation of a request message. On the top the transmitted channels packets are decoded [R, G, B, V].

ISBN: 978-1-61208-987-4

III. EXPERIMENTAL EVALUATION

In Figure 7, it is displayed the normalized MUX signals and the decoded messages assigned to IM received by Vehicle *a*, *b* (Figure 7a) and *c* (Figure 7b) at different response times. On the top the transmitted channels packets [R, G, B, V] are decoded. In the right side, the received channels for each vehicle are identified by its 4-digit binary codes and associated positions in the unit cell.

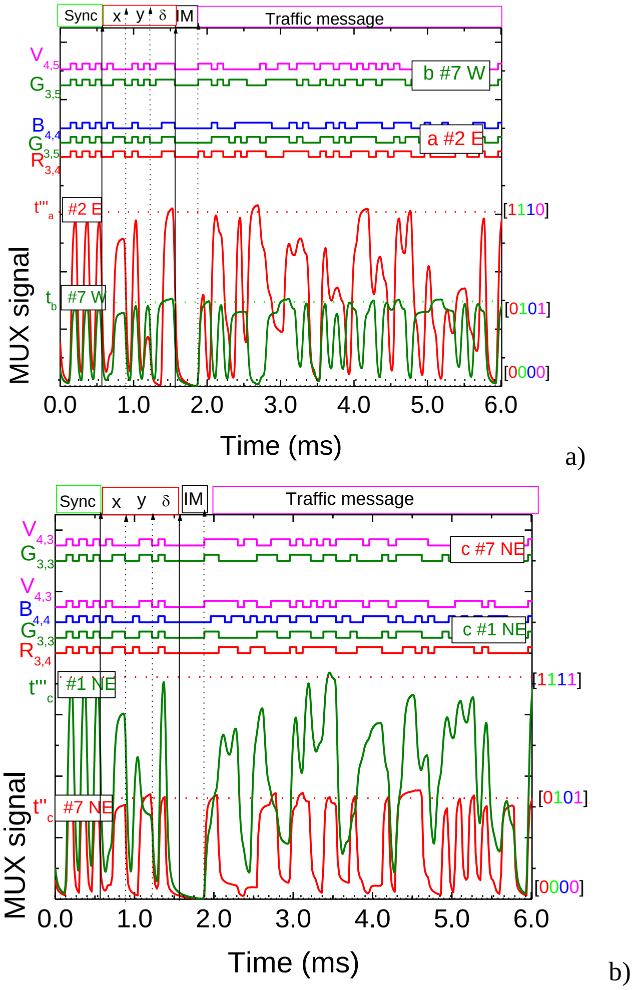

Figure 7 Normalized MUX signal responses and the assigned decoded messages acquired by vehicles *a*, *b* and *c* at different response times. On the top the transmitted channels packets [R, G, B, V] are decoded. a) Vehicle *a*, pose #2E, and vehicle *b*, pose #7W). b) Vehicle c, poses #7NE, #1NE.

Results show that, as the receiver moves between generated point regions, the received information pattern changes. Taking into account Figure 4 and Figure 6, Vehicle *a*, driving the right lane enters the response distance by #2 (t'_a, Phase1, green pose), goes straight to E. Then, this vehicle enters the crossroad through #8 (t''_a) and leaves it in the exit #2 at t'''_a, as displayed in the figure, keeping always the same direction (E). Vehicle *b* after crossing Intersection 2, approaches the Intersection 1, asked permission to cross it (t_b) and receives authorization when the vehicle *a* left the intersection (end of Phase 2, t'''_a). Then, Phase 3 begins with vehicle *b* heading to the intersection (W) (pose red) while vehicle *a* follows it destination towards E (green pose). In Figure 7b, signal responses and the assigned decoded messages from vehicle *c* inside the intersection are displayed at t''_c and t'''_c. Data shows that vehicle *c*, driving in the in the left lane, receives order to enter the intersection in # 7, turning left (NE) and keeps moving in this direction across position #1 toward the North exit (Phase 2, violet pose).

In both intersections, before the request of vehicle *d* to cross Intersection 1, the IM is aware through the request made by its leader *c* that a follower is approaching (*d*). Three actions must be taken to promote smooth movement avoiding congestions and delays: changing the synchronism of intersection 2, delaying the passage of vehicles *b* and finally, allowing the joint passage of vehicles *b* and *d* at Intersection 1 in the same phase (Phase 3).

Based on the simulated traffic scenario (Figure 4) and using the concept of V-VLC queue/request/response messages (Figure 3) a phasing diagram was drawn and reported in Figure 8.

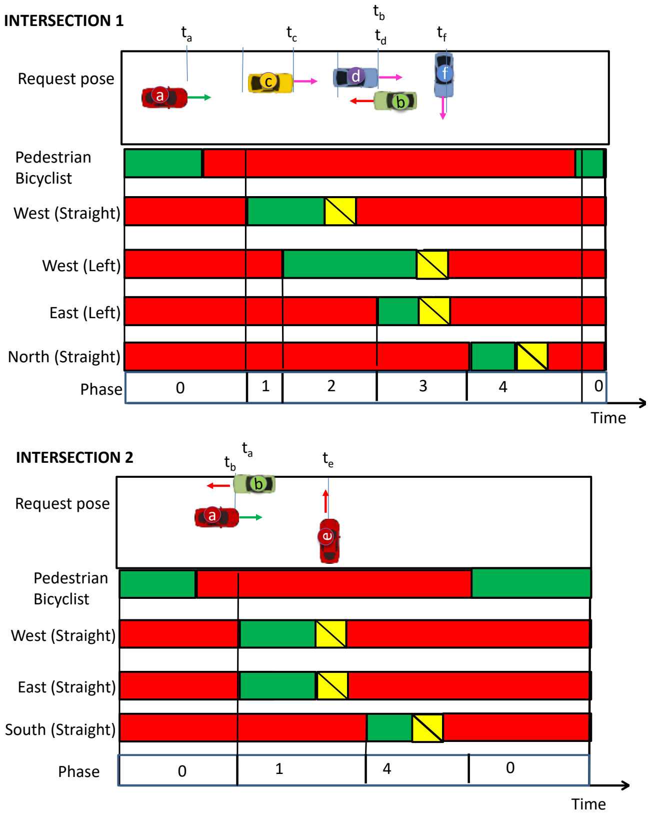

Figure 8 Requested phasing of traffic flows

The traffic controller uses queue, request and response messages, from the *a*, *b*, *c*, *d*, *e* and *f* vehicles, fusing the self-localizations $q_i(t)$ with theirs space relative poses $q_{ij}(t)$ to generate phase durations appropriate to accommodate the demand on each cycle. The driving Vehicle *x* with its pose representation is assigned a unique time to enter the intersection, *t[x]*. According to the phasing diagram (Figure 3), in Figure 8, the phasing flow for the split intersection is visualized: Intersection 1: Phases 0, pedestrian/bicyclist phase, Phase 1 (W straight flow), Phase 2 (W straight and left flows), Phase 3 (W and E left flows), Phase 4 (N straight flow); Intersection 2: Phases 0, pedestrian/bicyclist phase, Phase 1 (W and East straight flows), Phase 4 (S and right-turn approach flow. The exclusive pedestrian and bicyclist stage, “Walk” interval begins in both at the end of Phase 4.

IV. CONCLUSIONS

Using V-VLC-ready connected cars, we propose a queue/request/response approach for managing split intersections. A communication scenario is stablished and a “mesh/cellular” hybrid network configuration proposed. As a PoC, a phasing of traffic flows is suggested. In this study, the vehicles' arrival is controlled and they are scheduled to cross intersections at predetermined times to minimize traffic delays. V2I2V communication provides real-time data on queues, requests, and messages distances, including queue, request, and message travel times that influence traffic channeling in various routes. Compared with radio transceivers and directional antennas used in connected cars, visible light provides more accurate distance and position measurement thanks to its high directivity. Based on the simulated/experimental results, the proposed VLC cooperative architecture appears to be appropriate for the intended applications. The introduction of VLC between connected vehicles and the surrounding infrastructure allows the direct monitoring of critical points that are related to the queue formation and dissipation, relative speed thresholds and inter-vehicle spacing increasing the safety.

ACKNOWLEDGEMENTS

This work was sponsored by FCT – Fundação para a Ciência e a Tecnologia, within the Research Unit CTS – Center of Technology and Systems, reference UIDB/00066/2020.

REFERENCES

[1] S. Yousefi, E. Altman, R. El-Azouzi, and M. Fathy, "Analytical Model for Connectivity in Vehicular Ad Hoc Networks," IEEE Transactions on Vehicular Technology, 57, pp.3341-3356 (2008).

[2] D. Elliott,W. Keen, and L. Miao, “Recent advances in connected and automated vehicles” Journal of Traffic and Transportation Engineering, Vol. 6, Issue 2, pp.109-131(April 2019).

[3] N. Jitendra and Bajpai, “Emerging vehicle technologies & the search for urban mobility solutions,Urban, Planning and TransportResearch, 4:1, pp.83-100, DOI: 10.1080/21650020.2016.1185964(2016).

[4] N. Wang, Y. Qiao, W. Wang, S. Tang, and J. Shen, “Visible Light Communication based Intelligent Traffic Light System: Designing and Implementation,”2018 Asia Communications and Photonics Conference (ACP) DOI: 10.1109/ACP.2018.8595791(2018).

[5] N. Cheng, et al. “Big data driven vehicular networks,” IEEE Network, vol. 32, no. 6, pp.160–167, (Nov. 2018).

[6] P. Singh, G. Singh, and A. Singh, “Implementing Visible Light Communication in intelligent traffic management to resolve traffic logjams Int. J. Comput. Eng. Res, 5(9), pp.1-5 (2015).

[7] D. O’Brien, et al. “Indoor Visible Light Communications: challenges and prospects,” Proc. SPIE 7091, 709106, pp. 60-68 (2008).

[8] H. Parth. X. Pathak, H. Pengfei, and M. Prasant,”Visible Light Communication, Networking and Sensing: Potential and Challenges,” September 2015, IEEE Communications Surveys & Tutorials 17(4): Fourthquarter 2015, pp. 2047 – 2077 (2015).

[9] T. Nawaz, M. Seminara, S. Caputo, L. Mucchi, and J. Catani, ‘‘Low-latency VLC system with Fresnel receiver for I2V ITS applications,’’ J. Sensor Actuator Netw., vol. 9, no. 3, p. 35, Jul. 2020.

[10] S. Caputo, et al. ‘‘Measurement-based VLC channel characterization for I2V communications in a real urban scenario,’’ Veh. Commun., vol. 28, Apr. 2021, Art. no. 100305.

[11] M. A. Vieira, P. Louro, M. Vieira, A. Fantoni, and A. Steiger-Garção, “Light-activated amplification in Si-C tandem devices: A capacitive active filter model,” IEEE sensor journal, 12(6), 1755-1762 (2012).

[12] M. A. Vieira, M. Vieira, P., Vieira, and P. Louro, “Optical signal processing for a smart vehicle lighting system using a-SiCH technology,” Proc. SPIE 10231, Optical Sensors 2017, 102311L (2017).

[13] P. Pribyl, M. Pribyl, Lom, and M. Svitek, ‘‘Modeling of smart cities based on ITS architecture,’’ IEEE Intell. Transp. Syst. Mag., vol. 11, no. 4, pp. 28–36, Nov. 2019.

[14] R. Miucic, “Connected Vehicles: Intelligent Transportation Systems.” Cham, Switzerland: Springer, 2019.

[15] M. Vieira, M. A. Vieira., P. Louro., P. Vieira, A. Fantoni, “Light-emitting diodes aided indoor localization using visible light communication technology,” Opt. Eng. 57(8), 087105, 2018.

[16] M. A. Vieira, M. Vieira, P. Louro, P. Vieira, "Bi-directional communication between infrastructures and vehicles through visible light," Proc. SPIE 11207, Fourth International Conference on Applications of Optics and Photonics, 112070C (3 October 2019); doi: 10.1117/12.2526500. 2019.

[17] Y. Zhu, W. Liang, J. Zhang, and Y. Zhang, “Space-Collaborative Constellation Designs for MIMO Indoor Visible Light Communications,” IEEE Photonics Technology Letters, vol. 27, no. 15, pp. 1667–1670, 2015.

[18] S. Momeni and B. E. Wolfinger, “Availability evaluations for IPTV in VANETs with different types of access networks”. EURASIP Journal on Wireless Communications and Networking, Springer Open Journal, 2014:117, 2014.

[19] M. A. Vieira; M. Vieira; P. Vieira, and P. Louro. “Optical signal processing for a smart vehicle lighting system using a-SiCH technology,” Proc. SPIE. 10231 Optical Sensors 2017, 102311L. (2017).

[20] M. A. Vieira; M. Vieira; P. Louro, and P. Vieira, "Cooperative vehicular communication systems based on visible light communication," Opt. Eng. 57(7), 076101 (2018).

VLC Footprint maps for Positioning and Guidance

Paula Louro, Manuela Vieira, Manuel Augusto Vieira
DEETC/ISEL/IPL
R. Conselheiro Emídio Navarro, 1959-007
Lisboa, Portugal

CTS-UNINOVA
Quinta da Torre, Monte da Caparica, 2829-516,
Caparica, Portugal
e-mail: plouro@deetc.isel.pt, mv@isel.ipl.pt,
mvieira@deetc.isel.pt

***Abstract*— Visible Light Communication (VLC) is currently a research topic due to the possibility to handle the general, worldwide demanding need for communication. VLC uses Light Emitting Diodes (LED), operating in the visible part of the electromagnetic spectrum, as optical sources for optical wireless communication. The technology simultaneous lighting and communication, providing high data rates, reliability and a secure data transmission compared to other wireless technologies (such as Wi-Fi). This paper explores the use of VLC to establish different optical communication links for bidirectional communication between vehicles and infrastructures, using 2 links, namely Infrastructure-To-Vehicle (I2V) and Vehicle-To-Infrastructure (V2I) communication. The proposed application uses VLC to support autonomous navigation of mobile robots inside an automated warehouse, providing guidance and management services. Specific coding schemes are used in each optical link. In the I2V link, RGB white LEDs are used to allow simultaneous modulation of the emitters embedded in each LED, which enables wavelength division multiplexing of the transmitted optical signals. The detection is based on an a-SiC:H pin-pin photodetector with tunable sensitivity in the visible range. Different indoors communication scenarios are presented and bit error rate is discussed using a parity check bits for error control.**

Keywords- Visible Light Communication; Indoor guidance; White LEDs; Lambertian model; navigation cell.

I. INTRODUCTION

Indoor positioning can be addressed by several techniques, such as Wi-Fi, Assisted GPS (A-GPS), Infrared, Radio Frequency Identification (RFID), and many other technologies [1][2]. Visible Light communication (VLC) is also an alternative, enhanced accuracy technology. VLC operates with visible light extending from 400 nm up to 750 nm [3][4]. VLC systems use modulated LEDs to transmit information [5]. Due to its characteristics, LEDs [6] can be switched very fast to produce modulated light in high frequencies, allowing data transmission in high speed. For lighting purposes, energy saving demands the use of white LEDs [7][8], either based on blue emitter coated with a phosphor layer or based on polychromatic emitters. Phosphor-based LEDs usually consist of a blue LED chip covered in a yellow phosphor layer. Due to the long relaxation time of the phosphor, when this LED is used for VLC, the modulation bandwidth is limited, thereby limiting the transmission capacity. Using a blue filter before the receiver unit can increase the LED modulation bandwidth by eliminating the slow response of the yellow light component [9][10]. Although tri-chromatic LEDs are more expensive, they provide more bandwidth due to the independent modulation of each chip of a monolithic device.

The receiver unit of VLC systems usually include silicon based photodiodes, as these devices operate in the visible region of the spectrum, or CMOS image sensors [11][12].
In this paper we propose the use of a multilayered a:SiC:H [13] [14] device to perform the photodetection of the optical signals generated by white trichromatic RGB LEDs [15], [16]. The system was designed for positioning and guidance [17][18], and the transmitters of each white LED were specifically modulated at precise frequencies and coding bit sequences [19][20].

The proposed lighting and positioning/guidance system involves wireless communication, computer based algorithms, smart sensor and optical sources network, which constitutes a transdisciplinary approach framed in cyber-physical systems.

The paper is organized as follows. After the introduction (Section I), the general description of the system is presented in Section II. In Section III, the communication protocol and the encoding/decoding techniques are analyzed and discussed. At last, conclusions are addressed in Section IV.

II. VLC SYSTEM GENERAL DESCRIPTION

The VLC system is composed by the transmitter and the receiver modules, located at the infra-structure and at the mobile vehicle. Two optical links are established between the lamps and the vehicles, for I2V and V2I transmission. The optical source of the transmitter at infrastructure consists of four white RGB LEDs, while at a vehicle it is a multicolor LED or a single-color LED placed at the top. The sensor device used for the detection of the optical signals is a monolithic heterojunction composed of two pin structures [21]. As a result of its narrow thickness (200 nm) and higher bandgap (2.1 eV), the front pin a-SiC:H photodiode is responsible for the device's sensitivity to short wavelengths of the visible range (400 - 550 nm). The back pin a-Si:H structure operates in the complementary past of the visible range, collecting the long wavelengths (520 nm - 700 nm) [22]. The illumination window is established on the front photodiode. The use of steady state light as background light provides an enhancement of the electrical field of the front pin photodiode and the amplification of the generated photocurrent signal due to long wavelength light.

A. *Transmitter configuration*

For every channel of the I2V and V2I links, synchronous transmission based on a 64 bits data frame was used. In Figure 1, it is displayed the configuration of the LED lamp with four RGB white LEDs used in the I2V link. A uniform white light is provided in the indoor area by all three emitters (red, green, and blue). However, only specific emitters are modulated at a frequency imperceptible to the human eye. Each of these lamps illuminates an area with full radial coverage as shown in Figure 1.

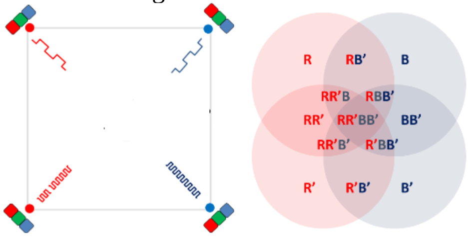

Figure 1. Configuration of the VLC emitter: a) 4 RGB white LEDs; b) coverage area of each modulated emitter.

The illuminated area corresponds to the coverage area of each lamp, defining a unit cell for the vehicle navigation along the space. The modulated emitters are the red junctions of the LEDs placed at the left side and the blue junctions of the LEDs at the right side.

B. *Footprint map*

In each unit navigation cell, any receiver will be able to identify the emission lamp and make a correspondence to the spatial position inside the warehouse. By modulating the red and blue emitters of each lamp, the optical pattern created within each navigation cell can enhance position accuracy. Inside the navigation cell, top emitters (labelled R and B) point north, bottom emitters (R' and B') point south, and left (R and R') and right (B and B') emitters point west and east, respectively. Based on this assumption, the RB' optical pattern corresponds to the north direction, R'B' to the south, RR' to the west and BB' to the east. The intercardinal directions inside the navigation cell correspond to RR'B (northwest), RBB' (northeast), RR'B' (southwest) and R'BB' (southeast).

Using adjacent LED lamps to light the indoor space, different navigation cells are enabled by each lamp. Every navigation cell contains 3 racks in each direction (forward and reverse) of the movement. The information transmitted by each set of four RGB LEDs includes the spatial location and information on the available items of the racks under their coverage area.

C. *Coding*

In Figure 2, it displayed the data frame structure the bi-directional communication I2V and V2I.

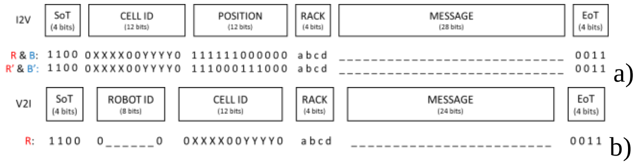

Figure 2. Data frame structure the communication: a) I2V and b) I2V channels.

Data frames are words of 64 bits composed each of six blocks. First and last blocks, labelled respectively as SoT and EoT are used to trigger synchronization of the transmitter and receptor in each link.

In the I2V link, there are also the blocks CELL ID, POSITION, RACK and MESSAGE. Identification of the unit cell is given by the block CELL ID. The format of the word code is 0XXXX00YYYY0, where XXXX addresses the line and YYYY the column of the unit navigation cell. Block POSITION provides information about which emitters are being detected by the mobile vehicle and thereby enables the vehicle to know its relative position within the navigation cell. The block RACK contains information about the stock stored inside the rack, addressing different sections. The MESSAGE block (32 bits) enables the possibility of transmitting a random message to the vehicle.

In the V2I link, a single LED is used to transmit information from the vehicle to the infrastructure, namely information about items being removed from the rack within the navigation cell to the shipping station. The code word contains the blocks ROBOT ID, CELL ID, RACK and MESSAGE, besides SoT and EoT blocks. The blocks ROBOT ID and CELL ID encode the identification of the transmitting vehicle and of the receiver infrastructure, The RACK block identifies the specific rack from where items are being removed and the MESSAGE block encodes the item and quantity being removed.

III. RESULTS AND DISCUSSION

In the V2I link, a single emitter is used to transmit information from the mobile robot to the LED infrastructure. In Figure 3, it is displayed the output signal due to the optical signal transmitted by the mobile robot after removing items from a specific rack. On the top it is displayed the optical signal with the transmitted bit sequence. As this V2I link uses a single emitter is used in this link, the photocurrent signal, when under line of sight condition, follows the pattern of the single transmitted optical signal. Thus, decoding is a simple process, limited only by the photodiode sensitivity at low illumination conditions.

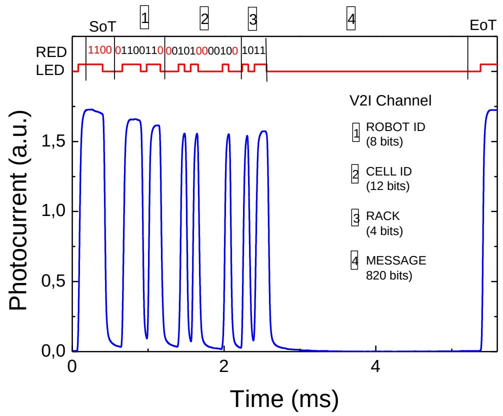

Figure 3. Output signal transmitted by the robot to the infrastructure after removal of items from the rack. On the top it displayed the transmitted optical signal.

As shown in the figure, bits in red color, either set to 1 or to 0, cannot be changed in this channel. Bits in black color are those that define the specific communication conditions. In this case, the blocks of the coded 64-bits word can be easily decoded. Bits of the ROBOT ID are 01100110, corresponding to the identification code 118 (decimal representation). The CELL ID provides for the decoded bits, the number 001010000100, which corresponds to line 5 and column 2. Bits of the RACK block are 1011, representing that items from the first and third racks were removed when the vehicle moved in the forward lane.

In the I2V link, the use of four emitters to transmit the coded information generates 16 photocurrents levels, assigned to 16 different optical excitations. These levels are dependent on the optical intensity at the reception end, however, its relative position is assumed to be constant. This, supports the use of a calibration curve to demultiplex the signal, decode the transmitted bits and enable identification of the input optical signals. In Figure 4, it is displayed the calibration curve, showing the 16 output levels assigned to each input optical state. The driving current of each LED emitter was adjusted to provide different levels of photo excitation.

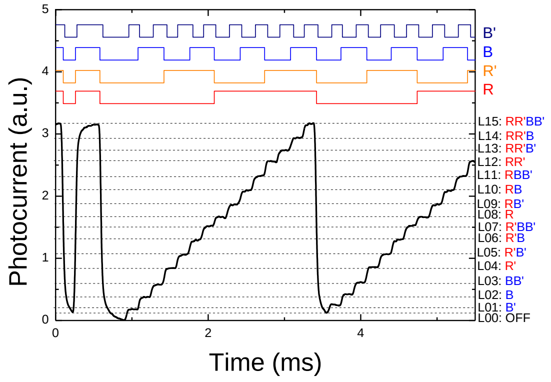

Figure 4. Calibration photocurrent signal using two red and two blue optical signals (on the top it is displayed the waveform of the emitters modulation state).

On the right side of the picture it is shown the label of the modulated emitters that correspond to each photocurrent level. The decoding methodology based on the calibration curve may result in some error mismatch when the photocurrent levels are too close. In order to increase the accuracy of the decoding task, bit error detection with parity check bits can be used. Parity bits (P1, P2, P3) assigned to the 4 transmission channels (R, R', B, B') are evaluated using a simple algorithm that sums up the bits transmitted by 3 of the channels:

$$\begin{aligned} P1 &= R + R' + B' \\ P2 &= R' + B + B' \\ P3 &= R + B + B' \end{aligned} \tag{1}$$

In Figure 5, it is displayed the parity check bits evaluated by equation (1) for the transmission of the bit sequences plotted in The parity check bits sequences (P1, P2 and P3) are transmitted, respectively, by the R, R' and B emitters.

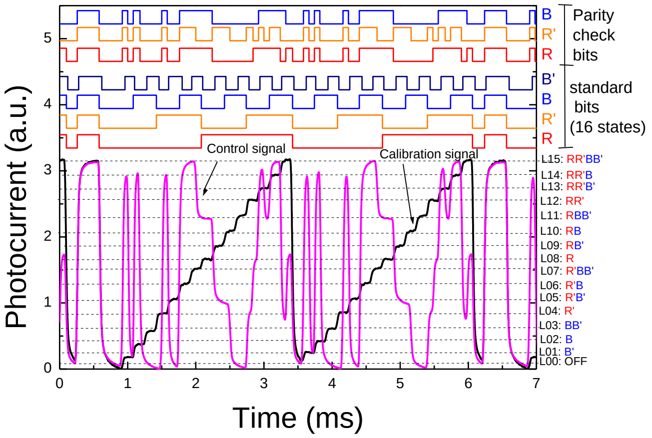

Figure 5. Calibration data and correspondent error control signal obtained by the transmission of the parity check bits.

Results show that the error control signal can be used to help on the decode process when photocurrent levels are very close. Under these circumstances, the use of parity check bits is able to detect and correct errors without the need to discard the transmitted data from the specific error bit and re-transmit it again.

In Figure 6, it is displayed the photocurrent signal acquired along the forward lane at positions under the coverage of RR'BB'. In superposition it is displayed the calibration grid. At the top it is displayed the input optical signals (R, R', B and B').

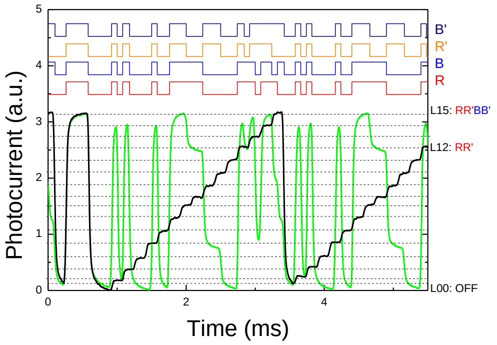

Figure 6. Photocurrent signal acquired along the forward path at cell central position under the coverage of RR'BB'.

The comparison of the output signal with the calibration curve allows the decode of the signal and identification of the receiver's position. Bit decoding of the multiplexed signal resulted for the CELL ID block the word 001010000100 (every 4 transmitters), corresponding to line 5 and column 2, for the POSITION block to the word 111111000000 from R and B transmitters and word 111000111000 from R' and B' transmitters, which indicates that the vehicle is at the center of the navigation cell. For the RACK block it is decoded the words 1110 from R and B transmitters and 1011 from R' and B' transmitters, which means that all racks of the cell are available with exception to the second rack in forward direction.

In Figure 7a), it is displayed the error control signal obtained with parity check bits of the transmitted signal of the I2V link shown in Figure 6.

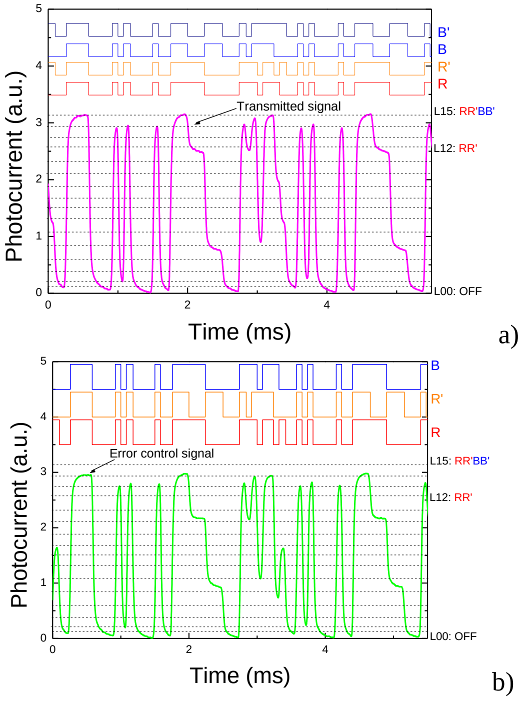

Figure 7. a) Transmitted signal by the I2V link and b) correspondent error control signal.

The use of the calibration curve for decoding the multiplexed signal, demands a periodic transmission of the 16 possible combination of the 4 optical signals to provide update of the calibration data and ensure correct output signal assignment. In this application, speed is not a critical issue, and this procedure does not overload the transmission efficiency. However, it can be discarded or done with less frequency, when the accuracy of the decoding is increased using parity check bits. The system is also feasible to be enhanced using feedback control for adjustment of the LED driving currents when the output photocurrent levels generated by the photodiode become too close. This procedure would minimize decoding errors due to parasitic effects such as optical intensity variations caused by to multiple reflections, light dispersion or other light sources.

IV. CONCLUSIONS

Bi-directional communication using VLC in both downlink and uplink channels has been addressed in a autonomous vehicle guidance system. The proposed indoors application deals with infrastructure to vehicle (I2V) and vehicle to infrastructure (V2I) communication in a warehouse. The vehicle moves autonomously through the warehouse transporting goods from the carts to the packaging station. The transmitted data is encoded in a 64 bits word, defined using specific data frames in communication channel. Codification of the optical signals ensured synchronization between frames. The code word of each channel was designed to ensure synchronization between frames, to transmit information of the transmitter identification and of spatial location. Experimental evaluation demonstrated that the decoding solution can provide robust communications, especially if automatic bit error control is implemented in the optical domain. This methodology will be used to support indoor positioning and guidance of autonomous guided vehicles operating in industrial environments, such as automated warehouses.

ACKNOWLEDGEMENTS

This work was sponsored by FCT – Fundação para a Ciência e a Tecnologia, within the Research Unit CTS – Center of Technology and systems, reference UID/EEA/00066/2020.

REFERENCES

[1] R. Mautz, “Overview of Current Indoor Positioning Systems”, Geodesy Cartogr., vol. 35, pp. 18–22, 2009.

[2] Y. Gu, A. Lo and I. Niemegeers, "A Survey of Indoor Positioning Systems for Wireless Personal Networks," IEEE Commun. Surv. Tutor., vol. 11, pp. 13–32, 2009.

[3] A. M. Căilean and M. Dimian, “Current Challenges for Visible Light Communications Usage in Vehicle Applications: A Survey”, IEEE Communications Surveys & Tutorials, vol. 19, no. 4, pp. 2681-2703, 2017.

[4] M. Z. Chowdhury, M. T. Hossan, A. Islam, and Y. M Jang, “A Comparative Survey of Optical Wireless Technologies: Architectures and Applications”, IEEE Access, vol. 6, pp. 9819-9840, 2018.

[5] G. Cossu, A. M. Khalid, P. Choudhury, R. Corsini, and E. Ciaramella, “3.4 Gbit/s Visible Optical Wireless Transmission Based on RGB LED,” Optics Express, vol. 20, pp. B501–B506, 2012.

[6] M. Kavehrad, "Sustainable Energy-Efficient Wireless Applications Using Light", IEEE Communications Magazine, vol. 48, no. 12, pp. 66-73, 2010.

[7] E. F. Schubert and J. K. Kim, “Solid-state light sources getting smart”, Science, vol. 308, no. 5726, pp. 1274-1278, 2005.

[8] J.-Y. Sung, C.-W. Chow, and C.-H Yeh, “Is blue optical filters necessary in high speed phosphor-based white light LED visible light communications?”, Optics Express, vol. 22, no. 17, pp. 20646-20651, 2014.

[9] H. Le Minh et al, “High-speed visible light communications using multiple-resonant equalization,” IEEE Photon. Technol. Lett., vol. 20, no. 14, pp. 1243–1245, 2008.

[10] A. M. Khalid, G. Cossu, R. Corsini, P. Choudhury, and E. Ciaramella, “1-Gb/s transmission over a phosphorescent white LED by using rate-adaptive discrete multitone modulation”, IEEE Photon. J., vol. 4, no. 5, pp. 1465–1473, 2012.

[11] Z. Zhou, M. Kavehrad, and P. Deng, “Energy efficient lighting and communications”, Proc. SPIE 8282, Broadband Access Communication Technologies VI, vol. 8282, pp. 82820J-1-82820J-15, 2012.

[12] A. Jovicic, J. Li, and T. Richardson, “Visible Light Communication: Opportunities, Challenges and the Path to Market”, IEEE Communications Magazine, vol. 51, no. 12, pp. 26-32, 2013.

[13] P. Louro, et al, “Optical demultiplexer based on an a-SiC:H voltage controlled device”, Phys. Status Solidi C, vol. 7, no. 3–4, pp. 1188–1191, 2010.

[14] P Louro, V Silva, I Rodrigues, M.A. Vieira and M Vieira “Transmission of Signals Using White LEDs for VLC Applications” - Materials Today: Proceedings, 3(3), 2016, pp. 780–787 doi:10.1016/j.matpr.2016.02.009.

[15] M. Vieira, M. A. Vieira, P. Louro, V. Silva, and P. Vieira, “Optical signal processing for indoor positioning using a-SiC:H technology”, Opt. Eng., vol 55, no. 10, pp. 107105-1-107105-6, 2016.

[16] M. A. Vieira, M. Vieira, P. Louro, and P. Vieira, "Cooperative vehicular communication systems based on visible light communication," Opt. Eng., vol. 57, no. 7, pp. 076101-, 2018.

[17] P. Louro; V. Silva; M. A. Vieira and M. Vieira, “Viability of the use of an a-SiC:H multilayer device in a domestic VLC application”, Phys. Status Solidi C, vol, 11, no. 11–12, pp. 1703–1706, 2014.

[18] P. Louro, J. Costa, M. Vieira, M. A. Vieira, and Y. Vygranenko, “Use of VLC for indoors navigation with RGB LEDs and a-SiC:H photodetector”, Proc. of SPIE, Optical sensors, vol. 10231, pp. 102310F-1-102310F-10, 2017.

[19] P. Louro, J. Costa, M. A. Vieira, and M. Vieira, “Optical Communication Applications based on white LEDs”, J. Luminescence, vol. 191, pp. 122-125, 2017.

[20] M. Vieira, M. A. Vieira, I. Rodrigues, V. Silva, and P. Louro, “Photonic Amorphous Pi’n/pin SiC Optical Filter Under Controlled Near UV Irradiation”, Sensors & Transducers, vol. 184, no. 1, pp. 123-129, 2015.

[21] M. A. Vieira, M. Vieira, P. Louro, L. Mateus andP. Vieira, Indoor positioning system using a WDM device based on a-SiC: H technology, Journal of Luminescence 191, 135-138.

[22] P. Louro, et al, MRS Proc. 2011, 1321, 223-228.

Development of a Lung Cancer Diagnosis Support System

Nelson Faria and Vítor Carvalho
2Ai, School of Technology
Polytechnic Institute of Cávado and Ave
Barcelos, Portugal
e-mail: a14805@alunos.ipca.pt; vcarvalho@ipca.pt

Sofia Campelos
Institute of Molecular Pathology and Immunology
University of Porto
Porto, Portugal
e-mail: acampelos@ipatimup.pt

***Abstract*— Lung cancer is the leading type of cancer death worldwide, and a correct diagnosis in an early stage gives more possibilities for treatment. Whole Slide Images generated from glass slides can be analysed using Artificial Intelligence technologies to help pathologists. In this study, an overview of lung cancer is made, exploring the methodologies used to improve the histopathological diagnosis of lung cancer. These methods are composed of Detection and Classification phases. To detect the neoplastic cells, the Whole Slide Image is split into patches, and a convolutional neural network is applied to identify the tumour regions and generate a heatmap to highlight them. Then, the features are extracted from the cancerous regions and submitted in a classifier to determine the histologic type of tumour present in each patch. In addition, it is proposed a possible solution based on the literature review that could be used as an aid in the pathological diagnosis of lung cancer.**

Keywords- lung cancer; digital pathology; artificial intelligence; convolutional neural networks; whole slide images.

I. INTRODUCTION

On a global scale, lung cancer has been the type of neoplasia that causes the highest number of deaths and is the second most common in terms of new cases [1]. The principal cause of this cancer is smoking, and the presence of a tumour nodule is detected by performing a radiologic detection methodology like chest X-ray or computed tomography [2][3]. After that, a confirmatory pathologic diagnosis is usually made on small biopsy and cytology samples [4][5]. In fact, the detection of lung cancer in an early stage is extremely important because the sooner it is detected, the greater the chances of effective treatment and survival. However, in more than 50 % of the new cases, the tumour has already metastasized to different parts of the body. The reasons of late detection could be the lack of symptoms at early stage, and incorrect diagnosis of the symptoms, such as cough and wheezing [6]. With the emergence of whole slide imaging, which is the process of scanning microscopic glass slides to produce digital slides, pathologists are able to examine the Whole Slide Images (WSIs) on a computer which makes possible the integration of software to assist pathologists (Figure 1). In this way, this project aims to develop a system that could benefit patients and pathologists by making lung cancer diagnosis simpler, decreasing the time spent by pathologists making the diagnosis, and improving the accuracy of the results. This article is composed of 4 sections: Section 2 begins with a brief overview of lung cancer's physiopathology before focusing on lung biopsy. Then, image processing techniques applied in pictures of biopsy tissue samples will be investigated, followed by an examination of the use of artificial intelligence in lung cancer detection. In Section 3, it is described the proposed approach to a lung cancer detection and classification system. Finally, Section 4 presents the main conclusions and the next steps.

ss

II. LITERATURE REVIEW

This section presents the etiology, classification, and methodologies for lung cancer detection. In addition, artificial intelligence techniques that aim to assist pathologists in the lung cancer diagnosis process are analysed.

A. Lung Cancer: Etiology, Classification and Detection Methodologies

According to data collected by the World Health Organization, the number of deaths from lung cancer reaches 1.8 million and 2.21 million new cases in 2020, which, when compared to other types of cancer, makes this neoplasia responsible for the highest number of deaths in the world [7]. The age group with the highest lung cancer rate is above the 50 years old and, even though, the lung cancer appears in the lungs, it can metastasise to other organs in the human body [1]. Also, the principal cause of this type of cancer is smoking, however, other risk factors have been identified, such as previous respiratory diseases, exposure to occupational carcinogens (arsenic, asbestos, chromium, nickel, and radon), polycyclic aromatic hydrocarbons, human immunodeficiency, virus infection, and alcohol consumption [1]–[3].

Carcinomas are the most common type of lung cancer, and they are split into four types: Adenocarcinoma, Squamous Cell Carcinoma, Large Cell Carcinoma and Small Cell Lung Carcinoma. The most common is Adenocarcinoma which affects about 80 % of cases. Currently, there are different methods to detect lung cancer, such as chest x-ray, computed tomography, and magnetic resonance imaging, but when the initial detection method is in the field of radiology, a confirmation pathological diagnosis is followed by a transthoracic needle biopsy. The glass slides acquired in the biopsy will be analysed by the pathologists in a brightfield microscope, or through WSIs that were obtained by digitising the glass slides [1].

B. *Artificial Intelligence techniques applied to Lung Cancer*

The increased amount of data generated by clinical systems, as well as the computational capacity, enable the development of computational systems capable of facilitating the diagnosis process, improving the accuracy and moving faster to the final diagnosis.

According to literature [1][8][9], the analysis of lung cancer in WSIs can be split into two moments: Detection and Classification. Wang et al. [8] presented a model using Inception V3 that was capable of analyse adenocarcinoma WSIs, classify and give a prognostic value with an accuracy of 89.8 %. By using the sliding window method, the model searches the presence of tumour in patches of 300 x 300 pixels. In 2018, Coudray [9] also used Convolutional Neural Networks (CNNs) with Inception V3 for their model, but the sliding window mechanism was used for 512 x 512 pixels patches which resulted in an accuracy of 87 % [1][9]. Another study from Li et al. [10] used 256 x 256 pixels patches and cropped them with a stride of 196 pixels with the aim to ensure sufficient overlapping between adjacent patches. The samples were applied into different types of CNNs, where the higher accuracy was given by AlexNet when it was trained from scratch with 97 % of accuracy and by ResNet when the pre-trained strategy was used (93 %) [1]. According to a study published in 2019 by Yu et al. [11], they also used the different CNN types where each Whole Slide Image (WSI) was split into tiles with 1000 x 1000 pixels with a 50 % overlap. The best resulting accuracy achieved from the evaluated models was 93.5 % [1][11]. To overcome the limitation that states the need for annotations by a pathologist to get a better result, Chen et al. [12] designed a technique that, instead of getting tiles from the WSI, the WSI is given as input without being split, which resulted in an accuracy of nearly 93% for lung cancer detection [1][12].

The detection task is followed by the classification task and provides the generated heatmap and, by applying morphological operations as erosion and dilation in these maps, the distribution and shape are features that can be extracted for further analysis and classification [8]. These features are used as inputs for models that will classify the lung cancer type present (e.g., Adenocarcinoma, squamous cell carcinoma, etc.). While Wang et al. [8] selected features associated with survival outcomes and used a univariate Cox proportional hazard model with a penalty to prevent overfitting, Yu et al. [11] employed Naïve Bayes classifiers, Support Vector Machines (SVMs) with Gaussian, linear and polynomial kernels, and Breiman’s random forest that received the features as input and gave the predicted lung cancer types as output, obtaining as higher accuracy 85 % [1].

III. PROPOSED APPROACH

Following the reviewed authors' approaches and as shown in Figure 2, the system to be developed must be capable of executing two phases: the Detection and Classification of the tumour present in a WSI. In the detection phase, the system should load the WSI and retain all the WSI’s tiles that contain tissue samples according to a given size (512 x 512 pixels). Then, it will execute transformations in the tiles, such as Augmentation and Rotation, to obtain more samples for training. After that, the tiles will be used in a Deep Learning Neural Network to detect the tumour using features that indicate its presence like colour and area of the cells. At the end of the detection steps, the system will compile the tiles back to the WSI format, generate a heatmap and give the prediction. In the classification phase, it will extract characteristics like perimeter and texture of the tumour from the regions of interest, apply a classifier (ex.: SVMs) that will distribute them by lung cancer subtypes, and, finally, show the output prediction to the user.

IV. CONCLUSION

The development of systems for optimisation of the lung cancer diagnosis is an area that is growing and many studies of methods to improve the current process are emerging. Furthermore, the use of deep learning is showing good results in medical systems, such as the recently implemented breast cancer diagnostic support system. However, since it is a developing area, there are limited amounts of image datasets available that allow training the algorithms with the desired performance to the point of being reliable in clinical use. In this paper, a possible solution was proposed as a high-level approach based on the available studies, with the aim of assisting the pathologist in the first morphological approach to the lesion to optimise the diagnostic process. Further phases will include, among other things, a thorough examination of the AI approaches used and the creation of algorithms to assess the presence or absence of tumors in the photos being analysed.

ACKNOWLEDGMENT

The authors would like to thank to the National Lung Screening Trial, The Cancer Genome Atlas and the Genomic Data Commons Data Portal for the lung cancer datasets availability. This paper was funded by national funds (PIDDAC), through the FCT – *Fundação para a Ciência e Tecnologia* and FCT/MCTES under the scope of the projects UIDB/05549/2020 and UIDP/05549/2020.

REFERENCES

[1] N. Faria, S. Campelos, and V. Carvalho, “Cancer Detec - Lung Cancer Diagnosis Support System: first insights,” in Proceedings of the 15th International Joint Conference on Biomedical Engineering Systems and Technologies - Volume 3: BIOINFORMATICS, 2022, pp. 83–90.

[2] B. C. Bade and C. S. Dela Cruz, “Lung Cancer 2020: Epidemiology, Eti- ology, and Prevention,” Clinics in Chest

Medicine, vol. 41, no. 1. W.B. Saunders, pp. 1–24, Mar. 01, 2020, doi: 10.1016/j.ccm.2019.10.001

[3] N. Duma, R. Santana-Davila, and J. R. Molina, “Non–Small Cell Lung Cancer: Epidemiology, Screening, Diagnosis, and Treatment,” Mayo Clin. Proc., vol. 94, no. 8, pp. 1623–1640, Aug. 2019, doi: 10.1016/j.mayocp.2019.01.013.

[4] R. L. Keith, “Lung Carcinoma - Pulmonary Disorders,” *Merck Manuals Professional Edition*, 2020. [Online] [retrieved: June, 2022]. Available: https://www.merckmanuals.com/professional/pulmonary-disorders/tumors-of-the-lungs/lung-carcinoma#v923730

[5] A. El-Baz et al., “Computer-aided diagnosis systems for lung cancer: Challenges and methodologies,” International Journal of Biomedical Imaging, vol. 2013. 2013, doi: 10.1155/2013/942353.

[6] C. Goebel, C. L. Louden, R. McKenna, O. Onugha, A. Wachtel, and T. Long, “Diagnosis of Non-small Cell Lung Cancer for Early Stage Asymptomatic Patients,” Cancer Genomics and Proteomics, vol. 16, no. 4, pp. 229–244, 2019, doi: 10.21873/cgp.20128.

[7] World Health Organization, “Cancer,” 2021. [Online] [retrieved: June, 2022]. Available: https://www.who.int/news-room/fact-sheets/detail/cancer

[8] S. Wang et al., “Comprehensive analysis of lung cancer pathology images to discover tumor shape and boundary features that predict survival outcome,” Sci. Rep., vol. 8, no. 1, pp. 1–9, Dec. 2018, doi: 10.1038/s41598-018-27707-4.

[9] N. Coudray *et al.*, “Classification and mutation prediction from non–small cell lung cancer histopathology images using deep learning,” *Nat. Med.*, vol. 24, no. 10, pp. 1559–1567, Oct. 2018, doi: 10.1038/s41591-018-0177-5.

[10] Z. Li *et al.*, “Computer-aided diagnosis of lung carcinoma using deep learning - a pilot study,” Mar. 2018, [Online]. [retrieved: June, 2022]. Available: http://arxiv.org/abs/1803.05471.

[11] K. H. Yu *et al.*, “Classifying non-small cell lung cancer types and transcriptomic subtypes using convolutional neural networks,” *J. Am. Med. Informatics Assoc.*, vol. 27, no. 5, pp. 757–769, May 2020, doi: 10.1093/jamia/ocz230.

[12] C. L. Chen *et al.*, “An annotation-free whole-slide training approach to pathological classification of lung cancer types using deep learning,” *Nat. Commun.*, vol. 12, no. 1, pp. 1–13, Dec. 2021, doi: 10.1038/s41467-021-21467-y.

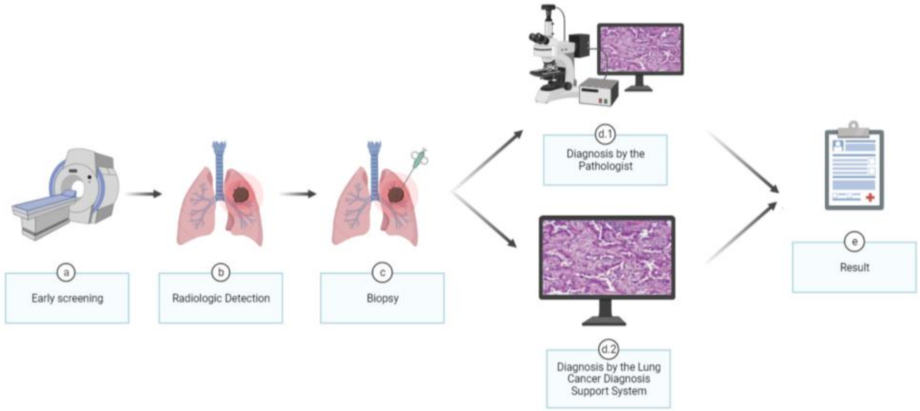

Figure 1. Actual Approach for Lung Cancer Diagnosis Support System.

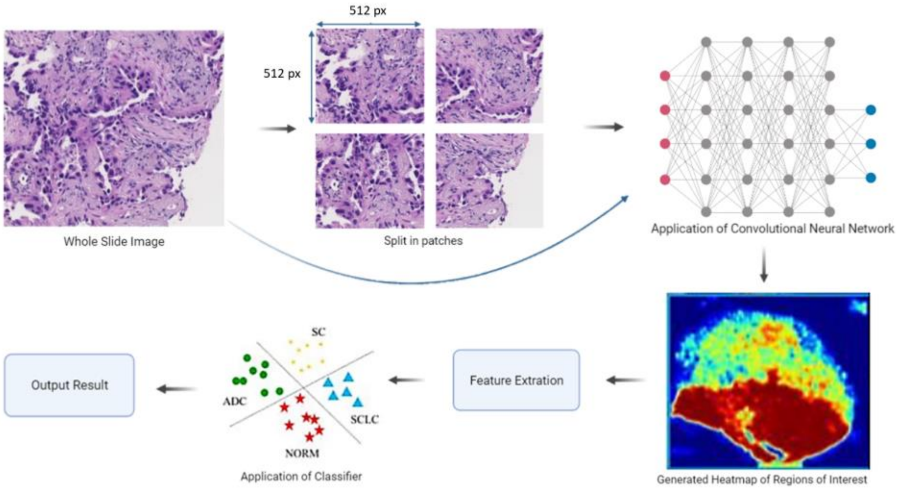

Figure 2. Diagram of the proposed approach to detect and classify the Lung Cancer according to a given WSI